

Nitrogen isotope evidence for stepwise oxygenation of the ocean during the Great Oxidation Event.

Chen Cheng, Vincent Busigny, Magali Ader, Christophe Thomazo, Carine Chaduteau, Pascal Philippot

▶ **To cite this version:**

Chen Cheng, Vincent Busigny, Magali Ader, Christophe Thomazo, Carine Chaduteau, et al.. Nitrogen isotope evidence for stepwise oxygenation of the ocean during the Great Oxidation Event.. Geochimica et Cosmochimica Acta, 2019, 261, pp.224-247. 10.1016/j.gca.2019.07.011 . hal-02270889

HAL Id: hal-02270889
https://hal.science/hal-02270889

Submitted on 14 Dec 2020

HAL is a multi-disciplinary open access archive for the deposit and dissemination of scientific research documents, whether they are published or not. The documents may come from teaching and research institutions in France or abroad, or from public or private research centers.

L'archive ouverte pluridisciplinaire **HAL**, est destinée au dépôt et à la diffusion de documents scientifiques de niveau recherche, publiés ou non, émanant des établissements d'enseignement et de recherche français ou étrangers, des laboratoires publics ou privés.

Nitrogen isotope evidence for stepwise oxygenation of the ocean during the Great Oxidation Event

Chen Cheng [a,b], Vincent Busigny [a,c,*], Magali Ader [a], Christophe Thomazo [d], Carine Chaduteau [a], Pascal Philippot [a,e]

[a] *Institut de Physique du Globe de Paris, Sorbonne Paris Cité, Université Paris Diderot, UMR 7154 CNRS, 75238 Paris, France*
[b] *China University of Mining & Technology, College of Geoscience and Surveying Engineering, 100083 Beijing, China*
[c] *Institut Universitaire de France, 75005 Paris, France*
[d] *Université de Bourgogne, Franche-Comté, UMR CNRS 6282 Biogéosciences, Dijon, France*
[e] *Géosciences Montpellier, CNRS-UMR 5243, Université de Montpellier, 34000 Montpellier, France*

Received 22 August 2018; accepted in revised form 4 July 2019; available online xxxx

Abstract

The Earth's oxygenation represents one of the most important environmental drivers of life's evolution, with the first rise, known as 'the Great Oxidation Event' (GOE), corresponding to unpreceded accumulation of atmospheric O_2, changes in the flux of marine nutrients and possibly global glaciations. However, the detailed evolution of the GOE is still debated, as for instance the accumulation trends of oceanic versus atmospheric oxygen and the nature of biogeochemical responses to oxygenation. Here, we combine organic carbon and bulk nitrogen isotope compositions with major element concentrations and iron speciation data of sedimentary rocks recovered from two drill cores (T2 and T3) in the early Paleoproterozoic Turee Creek Group, Western Australia, to track the redox evolution of marine conditions during the GOE. T2 core samples of the Kungarra Formation, which consists of clastic sedimentary rocks overlaid by the glaciogenic Meteorite Bore Member, were deposited ~2.31 Ga ago. T3 core intercepts, from bottom to top, quartzite of the Koolbye Formation, and shales and stromatolitic carbonates of the Kazput Formation, which were deposited around ~2.25 Ga. Samples from T2 show minor variations of $\delta^{13}C_{org}$ (avg. -34.5 ± 1.7‰, $n = 30$), with no significant difference between siliciclastic and glaciogenic sedimentary rocks. In contrast, T3 samples display an increase in $\delta^{13}C_{org}$ from -32.0 to -24.8‰ ($n = 54$) from shales to carbonates. In both T2 and T3 cores, $\delta^{13}C_{org}$ values are inversely correlated with Al_2O_3, suggesting a strong petrological control on $\delta^{13}C_{org}$ values, inferred here as resulting from variable contributions of detrital organic matter. Bulk N contents are low, from 13.5 to 56.7 ppm and 15.7 to 53.4 ppm in T2 and T3 samples, respectively. The $\delta^{15}N$ values show a bimodal distribution, with one mode at +2.6‰ in T2 and another at +8.8‰ in T3, independent from lithological variations. This $\delta^{15}N$ values shift between T2 and T3 is interpreted as reflecting a change from dominating N_2-fixers to NO_3-assimilating organisms. This implies an increase of NO_3^- availability, and thus of O_2 concentration, during the time interval separating the deposition of T2 and T3 sediments. Dissolved NO_3^- and O_2 concentrations of the Turee Creek marine basin are estimated from two models using N isotope data. The dissolved NO_3^- concentration has an upper limit ranging from 1.91 to 3.04 μM, about one order of magnitude below the average value of modern oceans. The lower limit for dissolved oxygen concentration ranges from 1.8 to 4.4 μM, which is two orders of magnitude lower than modern oceans. Together with previous studies, the present data

CORRECTED

* Corresponding author at: Institut de Physique du Globe de Paris, Sorbonne Paris Cité, Université Paris Diderot, UMR 7154 CNRS, 75238 Paris, France.
E-mail address: busigny@ipgp.fr (V. Busigny).

https://doi.org/10.1016/j.gca.2019.07.011

place quantitative constraints on the redox changes associated with the Great Oxidation Event and illustrate a stepwise increase of NO_3^- bioavailability between 2.31 to 2.25 Ga, in relation with increasing O_2 level.

Keywords: Nitrogen; Carbon; Isotopes; Oxygenation; Paleoproterozoic

1. INTRODUCTION

Deciphering atmospheric and oceanic oxygen levels throughout Earth's history is a central question in Geosciences since O_2 (1) tracked the evolution and activity of oxygenic photosynthesis, (2) led to the development of a protecting ozone layer in the stratosphere, absorbing high-energy UV light from the sun, (3) influenced the geochemical cycling of redox-sensitive elements through oxidative weathering, and (4) allowed the emergence of aerobic respiration among prokaryotes and eukaryotes as well as metazoans (Anbar and Knoll, 2002; Goldblatt et al., 2006; Lyons et al., 2014; Knoll and Nowak, 2017). The long-term evolution pattern of surface oxygen level is now considered as a multiple-stages process (Lyons et al., 2014), including a first stage with extremely low atmospheric O_2 concentration ($<10^{-5}$ PAL, present atmospheric level) in Archean Eon (>2.5 Ga), a second stage with rising atmospheric O_2 ($10^{-2} \sim 10^{-1}$ PAL) related to an oxygen overshoot during the Great Oxidation Event (GOE, $2.45 \sim 2.2$ Ga) in the Paleoproterozoic (Pavlov and Kasting, 2002; Bekker et al., 2004; Luo et al., 2016; Philippot et al., 2018), followed by declining atmospheric O_2 (10^{-3} PAL) in the Mesoproterozoic (Planavsky et al., 2014) and a last increase in atmospheric O_2 to near-modern level occurred during the Neoproterozoic Oxidation Event (NOE, $800 \sim 650$ Ma; Kah and Bartley, 2011; Planavsky et al., 2014). Despite this general agreement on the long-term evolution, the detailed timings, patterns and processes of oxygenation are still highly debated, such as the possibility of dynamic (Lyons et al., 2014) *versus* unidirectional (Kump, 2008) increase of atmospheric oxygen.

Nitrogen is a redox-sensitive element and is exchanged between atmosphere, hydrosphere, biosphere, crust and mantle through geological (*i.e.* sedimentation, metamorphism and volcanism) and biological (i.e. N-fixation, assimilation, nitrification, denitrification, anammox) processes (Goldblatt et al., 2009; Canfield et al., 2010; Sigman et al., 2010; Bebout et al., 2013; Zerkle and Mikhail, 2017). Nitrogen content and isotope composition of sedimentary rocks can be used to reconstruct nitrogen speciation and bioavailability through time (Galbraith et al., 2008), which are essentially controlled by the ocean redox structure (Ader et al., 2016). It is generally considered that N isotope composition of sedimentary rocks depends on (i) the relative contribution of N_2-fixers and nitrate or ammonium (*i.e.* fixed-N) assimilators to sedimentary organic matter (*e.g.* Kipp et al., 2018), (ii) the N isotope composition of available fixed-N, and utimately (iii) the oxygen and nutrient levels, which impact for instance the bio-available N species and the extent of N-fixation (*e.g.* phosphorus, Papineau et al., 2009, 2013). Nitrogen isotope signature of sediments can vary regionally as illustrated by the distribution of $\delta^{15}N$ values in the modern (Tesdal et al., 2013) and Precambrian (Ader et al., 2016) oceans. Nevertheless the identification of global changes in the N biogeochemical cycle through time can be assessed from systematic analyses of sedimentary rocks collected in various locations for a given time period. Over the last decade, large datasets of N isotope composition in Precambrian rocks have been acquired, and were compiled in recent reviews (Ader et al., 2016; Stüeken et al., 2016; Zerkle et al., 2017).

The evolution of marine N biogeochemical cycle during Earth's history has been tentatively subdivided into several stages according to N isotope data in greenschist and subgreenschist facies sedimentary rocks (Thomazo and Papineau, 2013; Ader et al., 2016; Stüeken et al., 2016). From Hadean to Mesoarchean (~2.8 Ga), the N biogeochemical cycle was anaerobic and N isotope signatures (mode at $\sim +1$‰) were dominated by Mo-based biological N_2-fixation (Stüeken et al., 2015a) but with heterogeneities in local basins due for instance to NH_4^+ assimilation under high concentration of dissolved NH_4^+ (Pinti et al., 2001, 2009) or alternative Fe-based/V-based nitrogenases used by N_2-fixers (Zhang et al., 2014). In the Neoarchean ($2.8 \sim 2.5$ Ga), moderately positive $\delta^{15}N$ values (mode at $\sim +3$‰; Garvin et al., 2009; Godfrey and Falkowski, 2009; Ader et al., 2016; Stüeken et al., 2016) appeared and were interpreted as episodic or localized aerobic nitrogen cycle (*i.e.* nitrification, denitrification, anammox) possibly caused by "oxygen oases" (Kendall et al., 2013). An extreme positive excursion of $\delta^{15}N$ values (up to +50‰) is recorded in some $2.6 \sim 2.7$ Ga sedimentary successions, and is interpreted either as partial NH_4^+ oxidation associated with quantitative denitrification of any nitrite or nitrate potentially generated (Thomazo et al., 2011) or as NH_3 degassing from alkaline lacustrine systems (Stüeken et al., 2015b). In the Proterozoic ($2.5 \sim 0.6$ Ga), heavy N isotope compositions (mode at ~+5‰; Ader et al., 2016; Stüeken et al., 2016) suggest an increasing activity of N aerobic pathways responsible for fixed-N losses (Jia and Kerrich, 2004; Papineau et al., 2009, 2013; Kump et al., 2011; Busigny et al., 2013; Stüeken et al., 2013; Godfrey et al., 2013; Ader et al., 2014; Koehler et al., 2017).

To date N isotope data in sedimentary rocks spanning the GOE ($2.45 \sim 2.2$ Ga) is sparse since only three studies explored the variations associated with this time period (Zerkle et al., 2017; Luo et al., 2018; Kipp et al., 2018). The first two focussed on the 2.31 Ga Rooihoogte and Timeball Hill formations in South Africa, and the last one targeted a suite of Paleoproterozoic marine sedimentary rocks ($2.4 \sim 1.8$ Ga). Zerkle et al. (2017) found highly variable but positive $\delta^{15}N$ values (+1.4 to +12‰), interpreted as an evidence for unstable but aerobic N biogeo-

chemical cycle, involving the presence of nitrate in the water column. Luo et al. (2018) provided extensive C and N isotope data on samples collected from multiple drillcores, and covering a larger time interval, where the $\delta^{15}N$ values (between −2 and +9‰) were interpreted as three main periods: (1) a pre-GOE period with NH_4^+ representing the dominant N source and being partially oxidized with subsequent quantitative denitrification, (2) a GOE period, recording a transitional increase of O_2, with quantitative nitrification and denitrification exhausting most of the bioavailable NH_4^+ and NO_3^- (implying that N_2 fixation served as the main source for biological N), and (3) a post-GOE period with NO_3^- availability in a predominantly oxygenated ocean. Kipp et al. (2018) observed a positive shift of nitrogen isotope ratios (+1.1 to +7.7‰), which supported that an expansion of oxygenated surface waters across the early Paleoproterozoic. These previous studies provide a first view of the N redox cycle during the GOE that needs to be extended to other sedimentary sequences worldwide in order to pin down the exact timing and mechanisms of this transition. In the present work, we analyzed bulk N and organic C concentrations and isotope compositions in sedimentary rocks from the Turee Creek Group, Western Australia, spanning the GOE from ~2.31 to ~2.25 Ga, to further understand temporal and spatial variations in the N biogeochemical cycling. The N data are coupled to major element concentrations and iron speciation data to evaluate potential detrital contribution, as well as diagenetic and/or metamorphic overprint, and then deduce the composition of primary authigenic organic matter. The N isotopic compositions are finally used in two models of N and O biogeochemical cycles in the water column to assess temporal paleo-redox variations in the basin.

2. GEOLOGICAL SETTING AND SAMPLES

The sedimentary rocks analyzed belong to the early Paleoproterozoic Turee Creek Group, Western Australia (Fig. 1). The Turee Creek Group conformably overlies the Boolgeeda Iron Formation, which represents the top of the Hamersley Group, and sits unconformably beneath sedimentary and volcanic deposits of the Wyloo Group (Martindale et al., 2015). The sedimentary sequence is characterized by a shallowing-upward marine succession from deep-water banded iron formation of the Boolgeeda, through fine-grained siliciclastic deposits and glaciogenic Meteorite Bore Member (MBM) of the Kungarra Formation, to fluvial and shallow marine strata of the Koolbye and Kazput formations (Martin, 1999; Van Kranendonk et al., 2015). The Turee Creek Group is remarkably well-preserved and experienced only limited metamorphic overprint, lower than greenschist facies ($T < 300$ °C; Smith et al., 1982; Rasmussen et al., 2005). The depositional time of the Turee Creek Group is constrained by two U-Pb zircon ages of 2,450 ± 3 Myr from the basal Boolgeeda Iron Formation (Woogarra rhyolites) and 2,209 ± 15 Myr from the base of the overlying Wyloo Group (Cheela Springs Basalt), respectively (Trendall et al., 2004). Recent *in situ* U-Pb dating of ~1500 zircons from these sequences confirmed that Boolgeeda Iron Formation is 2,460 ± 9 Myr old and provided a maximum age of 2,340 ± 22 Myr for the glacial deposits of Meteorite Bore Member (Caquineau et al., 2018). This age is in agreement with Re-Os dating performed on the bulk mudstone matrix and early diagenetic pyrites from the Meteorite Bore Member (MBM) glacial diamictites, which yielded an isochron age of 2,312.7 ± 5.6 Myr (Philippot et al., 2018).

In this study, we selected 85 samples (Table 1) from two pristine drill cores (T2 and T3) collected in the Hardey Syncline (Fig. 1a) of the Turee Creek Group at 22°50′49.70″S-116°52′27.70″E and 22°52′15.90″S-116°56′46.40″E (Fig. 1b), respectively. These two drill cores were sampled during the Turee Creek Drilling Project (TCDP) led by the Institut de Physique du Globe de Paris (IPGP). Drill core T2 intersected the Kungarra Formation between 384.9 and 117.7 m depth (see stratigraphic log in Fig. 3). The intercepted sedimentary succession consists of interbedded finely-laminated shale and siltstone between 384.9 and 281.7 m depth and is overlain by glacial diamictites of the Meteorite Bore Member between 281.7 and 117.7 m depth. The interbedded shale and siltstone show wavy beddings and cross-stratifications, with some occurrences of mud drapes. This indicates that the current flow at the time of deposition varied significantly, as for instance in storm-wave influenced shallow marine environment, tidal flats or delta settings. T2 core also comprises a massive sandstone deposit between 329.85 and 335.48 m depth and three laminated stromatolitic carbonates horizons at 351.10–351.55 m, 360.40–360.75 m and 384.2–384.5 m depths, respectively. The Meteorite Bore Member glacial diamictite consists of polymictic pebbles (carbonate, chert, gneiss) embedded in an homogeneous chlorite-rich mudstone matrix, with local siltstones and argillaceous layers. Drill core T3 intercepted the uppermost part of the shallow marine and fluvial sandstones of the Koolbye Formation between 189.3 to 182.4 m depth and the base of the Kazput Formation from 182.4 to 75.8 m depth (Fig. 3; Mazumder et al., 2015). From bottom to top, the Kazput Formation consists of laminated shales and siltstones up to 145.15 m depth, followed by massive bedded, oolithic and locally stromatolithic carbonates. From 106.15 m depth to the top of the core, the carbonates are progressively replaced by siltstones interleaved with argillaceous layers.

3. ANALYTICAL TECHNIQUES

All samples from the cores T2 and T3 were cut to cm-sized chips with fresh surface, cleaned with mQ water in ultrasonic bath and dried in an oven at 50 °C. The rock chips were then powdered to <60 μm in an agate mortar and homogenized. The analyses of carbon and nitrogen isotopes together with major element concentrations were performed on the same homogeneous powders.

Whole-rock concentrations of major elements were measured via ICP-AES at the Service d'Analyse des Roches et des Mineraux (SARM) of the Centre de Recherches Pétrographiques et Géochimiques (CRPG) of Vandoeuvre-Lès-Nancy, France, following the method described in Carignan et al. (2001). Analytical precision and detection

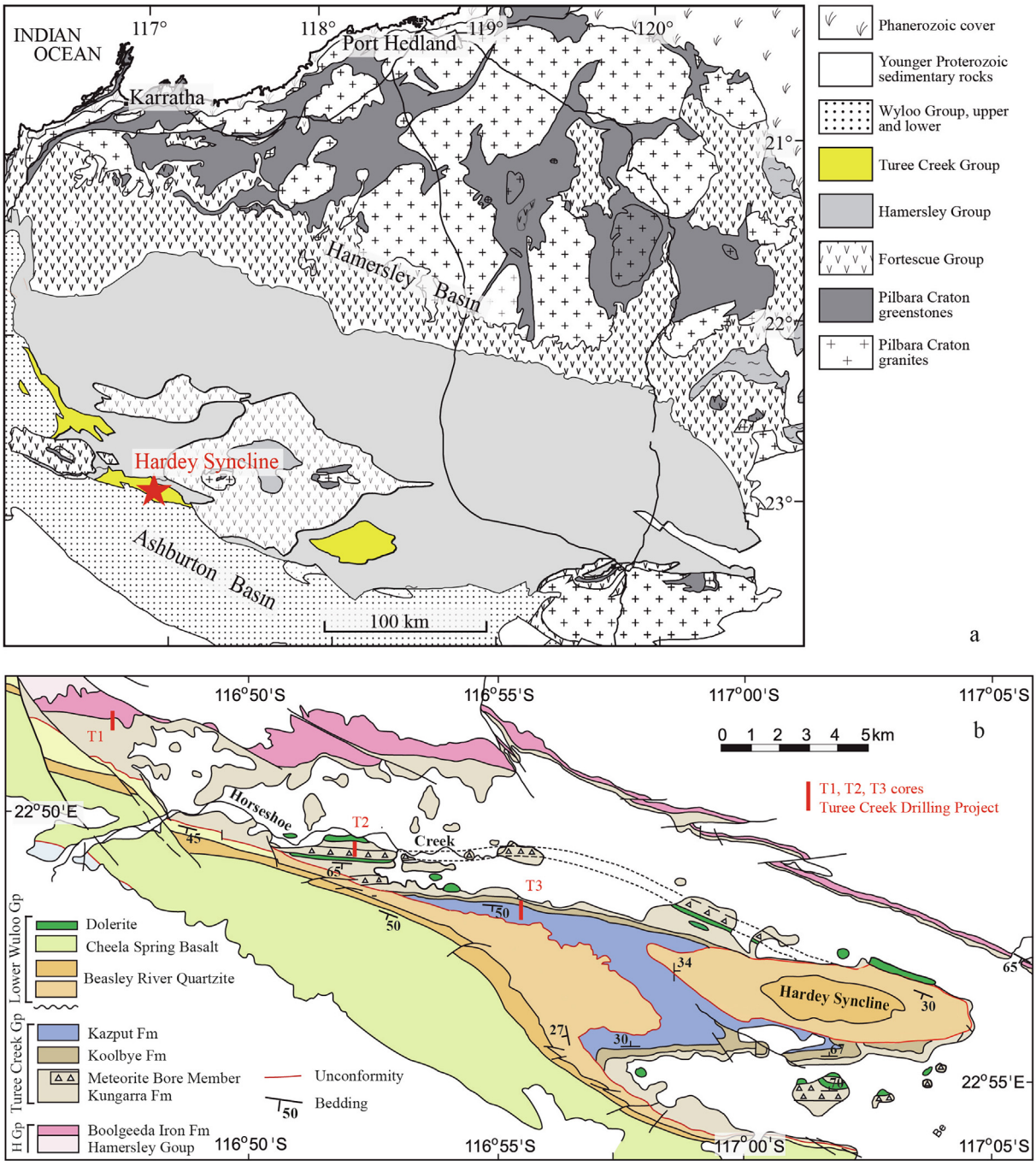


Fig. 1. Geological map of the Turee Creek Group in Western Australia (after Philippot et al., 2018). (a) Location of Hardey Syncline. (b) Location of T1, T2 and T3 drill cores.

limits for major element concentrations are typically better than ±10%.

Iron mineral species quantification follows the sequential iron extraction procedure proposed by Poulton and Canfield (2005). Four different mineral phases were extracted: (1) carbonate-associated Fe (Fe_{carb}); (2) Fe contained in oxyhydroxides (Fe_{ox}) including hematite, goethite, akaganeite, lepidocrocite and ferrihydrite; (3) magnetite (Fe_{mag}); (4) Fe bound to poorly reactive sheet silicates (Fe_{PRS}) including biotite, chlorite and glauconite. Each extracted species of iron described above was reacted with phenantroline and the concentration of the resulting Fe^{2+}-phenantroline complex was measured using a Jenways spectral photometer Series 67 at 515 nm, at the Biogeosciences Laboratory, following the method proposed in Reuschel et al. (2012) and described in details in Sauvage et al. (2013). The concentration of sulfur associated with pyrite (S_{py}) was determined from the chromium reducible

Table 1
Major element concentrations, organic carbon and bulk nitrogen contents and isotope compositions, and Fe/Al mass ratios in TCDP samples from T2 and T3 drill cores.

Sample	Rock Type	Depth*	TOC	N_{bulk}	$\delta^{13}C_{org}$	$\delta^{15}N_{bulk}$	C/N	Major elements (wt.%)										Fe/Al
		m	ppm	ppm	‰	‰	molar	SiO_2	Al_2O_3	Fe_2O_3	MnO	MgO	CaO	Na_2O	K_2O	TiO_2	P_2O_5	mass
Kazput Formation																		
T3 76.24–76.33	Shale	76.30	614	37.25	−28.99	8.07	19.2	63.27	14.06	7.04	0.72	3.29	2.07	0.86	2.89	0.60	0.10	0.66
T3 79.15	Shale	79.15	388		−28.82			59.49	14.50	7.37	0.81	3.70	2.68	0.82	3.04	0.61	0.09	0.67
T3 82.47–82.56	Shale	82.51	1294		−28.11			62.09	13.81	6.50	0.73	3.71	2.91	0.89	2.92	0.58	0.09	0.62
T3 86.28	Carbonate	86.28	320		−28.20			43.60	10.37	4.42	0.35	2.49	19.05	1.07	2.03	0.42	0.06	0.56
T3 89.06–89.15	Carbonate	89.10	307	16.20	−27.01	9.32	22.1	22.47	5.72	3.01	0.32	1.42	35.65	0.45	1.17	0.21		0.70
T3 91.70	Carbonate	91.70	270		−27.48			34.70	8.00	3.80	0.21	1.71	27.19	0.69	1.59	0.33	0.05	0.63
T3 93.45–93.55	Carbonate	93.50	471		−26.93			28.84	7.26	3.52	0.19	1.56	29.96	0.59	1.50	0.29		0.64
T3 95.96	Carbonate	95.00	375		−26.76			33.22	8.46	4.17	0.17	1.79	27.52	0.68	1.69	0.32	0.05	0.65
T3 98.44	Carbonate	98.44	669		−26.96			36.61	9.06	4.02	0.14	1.83	23.91	0.73	1.89	0.36	0.06	0.59
T3 100.52–100.62	Carbonate	100.57	315		−27.05			38.22	9.13	4.24	0.14	1.86	23.70	0.79	1.83	0.38	0.05	0.61
T3 102.62–102.71	Carbonate	102.68	487	28.26	−27.19	7.73	20.1	39.32	9.39	4.24	0.13	1.88	22.20	0.86	1.87	0.39	0.06	0.60
T3 103.35	Carbonate	103.35	397		−26.88			41.51	9.36	4.16	0.13	1.86	21.05	0.92	1.84	0.41	0.06	0.59
T3 105.18–105.32	Carbonate	105.25	535		−26.23			25.21	7.43	3.53	0.14	1.57	31.82	0.46	1.64	0.28	0.05	0.63
T3 107.77–107.84	Carbonate	107.80	293		−26.27			23.25	6.37	3.11	0.14	1.36	35.57	0.44	1.37	0.24	0.04	0.65
T3 108.65	Carbonate	108.65	656		−25.90			28.24	7.89	3.60	0.13	1.63	30.08	0.51	1.74	0.30	0.05	0.60
T3 109.76–109.84	Carbonate	109.80	348	23.85	−26.56	8.85	17.0	31.74	7.81	3.86	0.13	1.72	28.01	0.60	1.59	0.33	0.05	0.65
T3 115.09–115.19	Carbonate	115.14	472		−26.55			26.60	6.80	2.85	0.15	1.44	36.28	0.48	1.56	0.27	0.04	0.55
T3 116.37	Carbonate	116.37	359		−27.02			39.92	9.02	4.04	0.12	1.76	23.66	0.78	1.98	0.39	0.05	0.59
T3 118.23–118.31	Carbonate	118.27	379		−26.83			29.04	6.78	2.78	0.14	1.41	33.46	0.58	1.51	0.28	0.04	0.54
T3 120.73–120.84	Carbonate	120.78	419		−26.83			25.84	7.17	3.10	0.15	1.54	34.98	0.44	1.00	0.27	0.04	0.57
T3 123.82–123.90	Carbonate	123.88	1246	23.08	−26.72	9.01	63.0	27.52	6.98	2.97	0.15	1.48	34.68	0.50	1.61	0.28	0.04	0.56
T3 126.26–126.32	Carbonate	126.29	325		−26.56			23.54	6.26	2.59	0.15	1.34	37.93	0.41	1.48	0.24	0.04	0.55
T3 129.43–129.51	Carbonate	129.47	536		−26.59			22.06	6.54	2.52	0.17	1.35	38.16	0.39	1.63	0.23	0.04	0.51
T3 135.16–135.29	Carbonate	135.22	458		−27.45			31.89	8.26	3.23	0.19	1.66	30.68	0.60	1.96	0.32	0.05	0.52
T3 141.68–141.75	Carbonate	141.71	490		−28.74			28.20	7.52	3.25	0.37	1.71	36.76	0.60	1.72	0.29	0.05	0.57
T3 141.68–141.75#	Carbonate	141.71	377	23.13	−27.97	7.40	19.0	29.63	7.45	3.44	0.35	1.58	30.10	0.67	1.47	0.31	0.05	0.61
T3 144.34–144.47	Carbonate	144.40	579		−28.19			29.44	8.70	4.09	0.55	2.22	29.53	0.61	2.03	0.29	0.05	0.62
T3 144.80	Carbonate	144.80	507		−28.50			36.66	9.30	6.05	0.76	2.71	23.21	0.79	1.80	0.35	0.06	0.86
T3 149.19	Shale	149.19	425		−29.84			55.99	12.91	7.66	2.02	3.72	5.06	0.57	3.05	0.50	0.08	0.78
T3 151.52–151.61	Shale	151.57	782		−29.46			55.55	17.31	9.18	1.49	3.53	2.00	0.39	4.06	0.57	0.10	0.70
T3 151.52–151.61#	Shale	151.57	816	40.81	−29.29	9.89	23.3	54.86	16.90	8.67	1.42	3.25	2.15	0.24	3.89	0.57	0.09	0.68
T3 153.29	Shale	153.29	356		−29.34			50.72	11.26	6.94	7.10	3.93	7.21	0.45	3.50	0.52	0.07	0.82
T3 154.97	Shale	154.97	466		−29.05			42.37	12.94	7.16	5.54	3.90	8.53	0.47	3.96	0.47	0.09	0.73
T3 154.97–155.07	Shale	155.02	466		−29.05			59.28	15.42	6.85	2.18	2.86	3.01	0.52	3.57	0.62	0.07	0.59
T3 154.97–155.07#	Shale	155.02	548	32.50	−29.03	6.82	19.7	56.14	14.58	6.63	2.34	2.79	4.04	0.44	3.49	0.61	0.09	0.60
T3 155.07–155.19	Shale	155.13	559		−28.67			59.28	15.42	6.85	2.18	2.86	3.01	0.52	3.57	0.62	0.07	0.59
T3 156.54	Shale	156.54	375		−29.06			42.37	13.94	8.72	6.08	3.96	6.89	0.42	3.81	0.45	0.08	0.83
T3 157.26–157.35	Shale	157.30	893		−29.21			46.50	14.85	6.72	4.48	4.00	5.92	0.32	2.71	0.48	0.08	0.60
T3 157.26–157.35#	Shale	157.30	690	35.85	−29.14	9.27	22.5	44.50	14.37	8.08	4.50	3.88	6.72	0.27	3.36	0.46	0.09	0.74
T3 161.16–161.30	Shale	161.20	885		−30.16			48.32	16.01	9.58	2.42	4.47	5.17	0.48	3.81	0.48	0.10	0.79
T3 161.16–161.30#	Shale	161.20	872	45.75	−29.88	7.37	22.2	49.41	15.99	9.32	1.87	4.20	4.83	0.49	3.50	0.48	0.09	0.77

(*continued on next page*)

Table 1 (*continued*)

Sample	Rock Type	Depth*	TOC	N_{bulk}	$\delta^{13}C_{org}$	$\delta^{15}N_{bulk}$	C/N	Major elements (wt.%)										Fe/Al
		m	ppm	ppm	‰	‰	molar	SiO_2	Al_2O_3	Fe_2O_3	MnO	MgO	CaO	Na_2O	K_2O	TiO_2	P_2O_5	mass
T3 161.39	Shale	161.39	861		−29.76			50.51	16.93	10.29	1.61	4.53	3.63	0.53	2.00	0.48	0.11	0.80
T3 162.24–162.34	Shale	162.29	763		−29.60			42.87	13.98	8.70	2.21	4.71	8.69	0.88	3.63	0.40	0.08	0.82
T3 164.36–164.43	Shale	164.39	427		−29.81			43.87	12.21	27.88	0.51	4.91	2.39	0.22	0.00	0.38	0.14	3.02
T3 164.54	Shale	164.54	353		−28.59			33.99	7.52	29.01	1.53	4.46	6.94	0.02	0.00	0.24	0.23	5.10
T3 168.60	Shale	168.60	1264		−31.99			57.45	19.84	8.48	0.14	3.31	0.44	0.93	3.76	0.64	0.09	0.57
T3 170.64	Shale	170.64	473		−31.06			57.32	19.93	8.57	0.16	3.34	0.42	0.91	4.33	0.63	0.09	0.57
T3 171.65–171.71 Ca#	Shale	171.68	1131	44.92	−31.69	9.34	29.4	59.82	18.30	8.54	0.11	3.15	0.18	0.75	4.16	0.59	0.10	0.62
T3 171.71–171.80 Ag#	Shale	171.75	1338	53.42	−31.34	10.24	29.2	58.12	19.15	8.07	0.11	3.06	0.20	0.77	4.69	0.57	0.10	0.56
T3 174.22	Shale	174.22	1231		−30.27			54.15	16.76	13.77	0.85	4.35	1.82	0.90	2.36	0.46	0.16	1.09
T3 182.20–182.25	Carbonate	182.22	384		−26.15			5.20	1.50	6.85	9.77	10.57	26.32	0.03	0.00	0.07	0.09	6.04
T3 182.25	Carbonate	182.25	117		−24.77			13.54	1.58	26.28	7.00	5.99	14.13	2.56	2.94	0.04	0.11	21.94
Koolbye Formation																		
T3 183.70–183.77	Quartzite	183.73	169		−29.08			70.12	12.26	3.44	0.17	2.22	1.30	2.48	2.52	0.38	0.12	0.37
T3 186.98	Quartzite	186.98	67	15.72	−28.25	11.53	5.0	71.93	12.25	4.59	0.10	2.45	0.95	2.53	2.54	0.38	0.12	0.50
Meteorite Bore Member																		
T2 120.32	Diamictite	120.32	753	36.66	–33.09	4.25	24.0	65.36	15.22	7.38	0.05	2.24	0.66	1.46	2.93	0.65	0.11	0.64
T2 142.15	Diamictite	142.15	539		–33.59			65.62	15.18	7.15	0.05	2.16	0.41	1.43	2.96	0.64	0.11	0.62
T2 162.10	Diamictite	162.10	766	36.67	–33.22	3.82	24.4	66.60	15.13	7.09	0.05	2.07	0.81	1.51	3.02	0.64	0.12	0.62
T2 194.04	Diamictite	194.04	462		–33.51			68.17	14.07	6.55	0.05	1.95	0.77	1.43	2.58	0.61	0.12	0.62
T2 215.90	Diamictite	215.90	933	44.70	−34.60	1.64	24.4	60.46	17.35	9.05	0.05	2.64	0.47	1.12	3.06	0.70	0.12	0.69
T2 240.90	Diamictite	240.90	919		−34.77			62.58	16.67	7.98	0.05	2.38	0.36	1.27	3.26	0.69	0.11	0.63
T2 259.30	Diamictite	259.30	670	40.08	−34.74	4.10	19.5	63.14	16.01	7.59	0.05	2.29	0.53	1.24	3.10	0.64	0.11	0.63
T2 271.10	Diamictite	271.10	647		−34.75			66.16	15.14	7.35	0.05	2.24	0.76	1.41	2.57	0.62	0.11	0.64
T2 283.90	Diamictite	283.90	950		−35.31			65.07	16.34	7.90	0.05	2.46	0.30	1.62	3.09	0.79	0.11	0.64
Kungarra Formation																		
T2 299.70	Shale	299.70	1492	56.73	−36.27	2.11	30.7	56.52	20.32	9.21	0.05	2.91	0.25	1.01	3.96	0.48	0.12	0.60
T2 302.45	Shale	302.45	958		−35.80			63.44	15.76	7.88	0.05	2.46	0.37	1.52	2.80	0.69	0.09	0.66
T2 312.35	Shale	312.35	944		−35.84			65.26	15.13	8.10	0.05	2.50	0.26	1.56	2.38	0.69	0.10	0.71
T2 312.39	Shale	312.39	1241		−36.12			61.02	17.24	8.67	0.05	2.73	0.23	1.55	3.12	0.83	0.13	0.67
T2 324.80	Shale	324.80	747		−35.54			62.97	16.30	7.91	0.05	2.59	0.32	1.73	2.87	0.77	0.11	0.64
T2 329.73	Sandstone	329.73	213	37.56	−31.68	2.90	6.6	67.04	15.01	7.13	0.04	2.16	0.28	1.38	2.94	0.74	0.12	0.63
T2 333.10	Sandstone	333.10		32.50		−0.39		65.86	18.49	4.95	0.03	1.34	0.21	0.90	3.56	0.81	0.10	0.35
T2 333.65	Sandstone	333.65	62		−27.76			81.08	7.35	2.13	0.06	0.73	2.20	1.45	1.40	0.28	0.05	0.38
T2 335.55 Ca	Sandstone	335.55	251		–32.29			76.87	10.34	5.04	0.04	1.48	1.21	1.21	3.42	0.39	0.13	0.64
T2 335.55 Ag	Shale	335.56	663		−34.57			64.82	16.91	7.69	0.04	2.41	0.60	1.43	1.67	0.69	0.07	0.60
T2 347.45	Shale	347.45	1246		−35.69			60.03	18.37	8.63	0.05	2.77	0.30	1.31	3.63	0.60	0.11	0.62
T2 352.72	Shale	352.72	406		−34.76			65.76	13.55	7.81	0.08	2.34	1.84	1.37	2.17	0.59	0.12	0.76
T2 354.72	Shale	354.72	1066		−36.13			57.60	18.14	9.13	0.08	2.79	1.30	1.29	3.61	0.60	0.11	0.67
T2 359.43–359.50	Shale	359.46	857		−35.25			65.06	16.67	8.35	0.09	2.74	0.34	1.47	2.97	0.63	0.13	0.66
T2 359.45–359.60	Shale	359.53	1174		−35.04			63.31	17.57	8.84	0.10	2.85	0.37	1.34	3.14	0.64	0.13	0.67
T2 360.45	Shale	360.45	378	13.52	−34.30	3.98	32.6	46.79	8.57	4.84	0.68	1.98	17.38	1.51	1.07	0.48	0.10	0.75
T2 360.85	Shale	360.85	644		−34.90			62.23	13.09	7.12	0.18	2.60	3.33	1.49	2.09	0.74	0.12	0.72
T2 363.90	Shale	363.90	625	21.79	−34.15	−0.83	33.5	58.82	10.86	6.64	0.32	2.39	8.10	1.48	1.49	0.70	0.12	0.81

T2 369.68–369.73	Shale	369.68	1091		−35.40			62.16	17.85	8.57	0.06	2.77	0.21	1.35	3.38	0.70	0.12	0.64
T2 377.75	Shale	377.75	754		−34.58			57.65	18.89	10.73	0.06	3.38	0.29	0.80	3.56	0.52	0.14	0.75
T2 379.80	Shale	379.80	1090	35.92	−35.27	2.74	35.4	63.23	17.14	8.56	0.05	2.87	0.19	1.17	3.16	0.61	0.10	0.66
T2 384.60	Shale	384.60	945	21.20	−34.74	4.03	52.0											

* Depth in T2 and T3 drill core recovered by the Turee Creek Drilling Project (TCDP).

sulfur extraction by gravimetric quantification (Canfield et al., 1986). Iron associated with pyrite (Fe_{py}) was calculated from the S_{py} assuming stoichiometric ratio. The total iron concentration (Fe_T) has been measured as part of the ICP-AES analysis (see above). Because of their high reactivity toward hydrogen sulfide (Canfield et al., 1992; Poulton et al., 2004), the sum of Fe_{carb}, Fe_{ox}, Fe_{mag} and Fe_{py} are referred to as 'Highly Reactive' Fe fraction (Fe_{HR}) of the total iron concentration. Fe_{HR}/Fe_T ratio is then commonly used to argue for anoxic conditions when values are above a threshold of 0.38 (Raiswell and Canfield, 1998). Fe_{HR} enrichment, in excess toward this maximal detrital background, indicates an external source of reactive Fe decoupled from the siliciclastic flux. Euxinic conditions can also be identified when both Fe_{HR}/Fe_T and Fe_{py}/Fe_{HR} exceeds thresholds of 0.38 and 0.80, respectively.

Total organic carbon (TOC) content and isotope composition were determined on decarbonated samples. Carbonates from powdered samples were removed using 6 N HCl overnight at room temperature, followed by 2 h at 80 °C. The residue of acid attack was rinsed with distilled water and centrifuged several times until neutral pH was reached, and then dried at 50 °C for 2 days. After drying, the decarbonated powders were weighed and mass balance was done for subsequent calculation of the total organic C content. The powders were grounded again in an agate mortar to avoid any heterogeneity related to the analytical procedure of decarbonation. Aliquots of dried decarbonated samples (50–100 mg) were introduced in tin capsules and wrapped up. All capsules were analyzed on a Flash EA1112 elemental analyzer coupled to a Thermo Finnigan Delta^{plus} XP mass-spectrometer *via* a Conflo IV interface under a helium continuous flow. Three internal standards, calibrated against international standards, were used to calculate the $\delta\,^{13}C$ values of all samples. Replicate analyses on standards gave an external precision better than ±0.1‰ (1σ). Five different amounts of an internal standard were used to estimate total organic C content of the samples. The data were reported using the conventional δ unit (in permil) with respect to the V-PDB standard, such as $\delta^{13}C_{org} = [(^{13}C/^{12}C)_{Sample}/(^{13}C/^{12}C)_{V\text{-}PDB} - 1] \times 1000$. Up to four replicate analyses of each sample were performed for $\delta^{13}C_{org}$ measurements, but only the average values are provided herein. The reproducibility on samples TOC content and $\delta^{13}C_{org}$ values was always better than ±0.3 wt.% (1σ) and ±0.4‰ (1σ), respectively.

Bulk N content and isotope composition were measured on 24 samples selected to represent the various lithologies observed in the cores T2 and T3 (Table 1). The analyses were performed using sealed-tube combustion and on-line N_2 purification on an ultra-high vacuum line coupled to a triple-collector static mass spectrometer (Ader et al., 2006, 2014; Busigny et al., 2005, 2013). The procedure can be summarized as follows. The decarbonated samples (12–100 mg) embedded in pre-purified platinum foils were evacuated under vacuum at 300 °C for 12 h in quartz tubes filled with pre-cleaned CuO and Cu wires and CaO granules (Busigny et al., 2013). This degassing temperature was selected because metamorphic conditions of the Turee Creek Group did not exceed 300 °C (Smith et al., 1982;

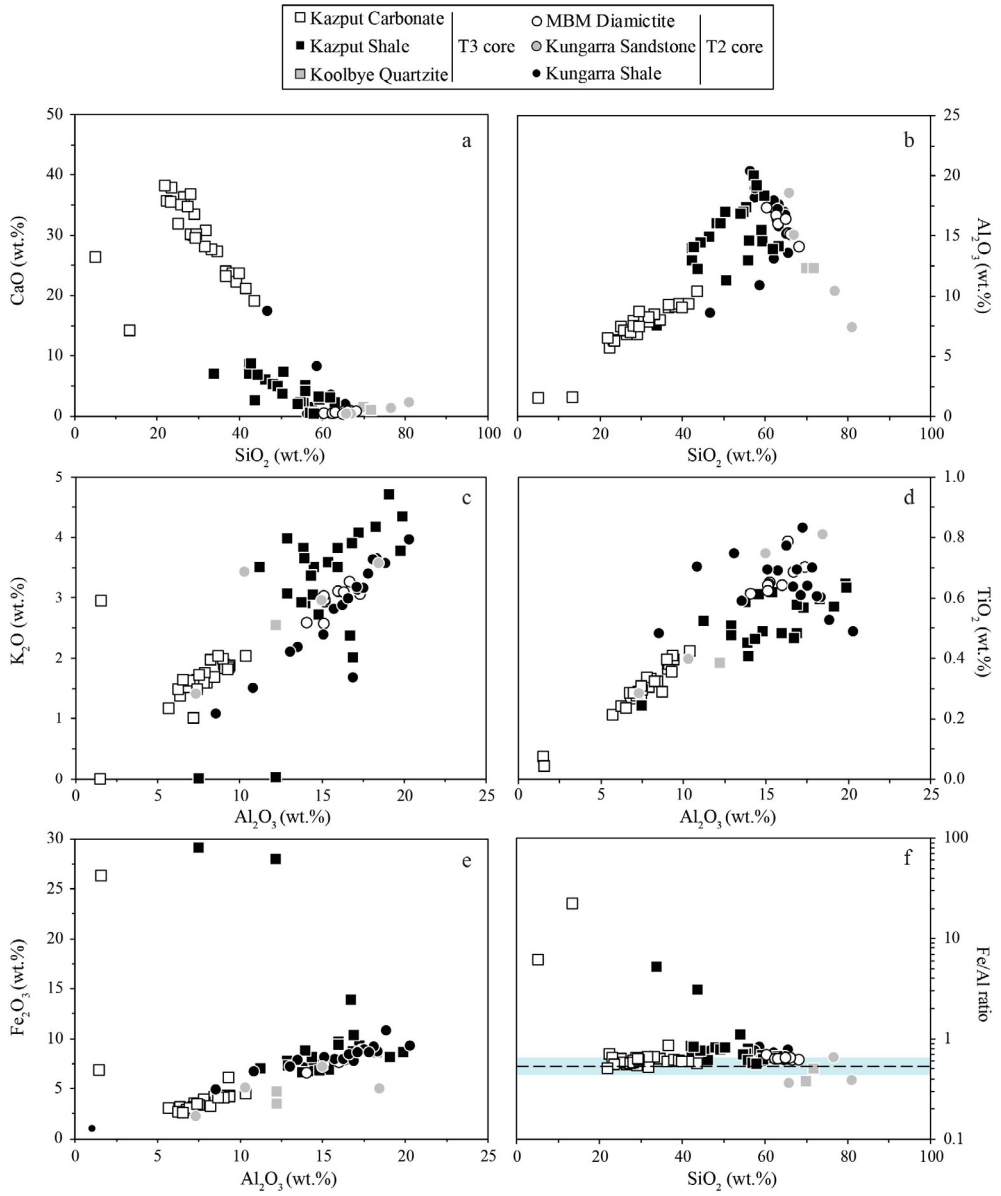


Fig. 2. Major element concentrations of the Turee Creek samples. Symbols represent the different lithological units from the two drill cores, T2 and T3 (MBM: Meteorite Bore Member). (a) CaO (wt.%) versus SiO_2 (wt.%). (b) Al_2O_3 (wt.%) versus SiO_2 (wt.%). (c) K_2O (wt.%) versus Al_2O_3 (wt.%). (d) TiO_2 (wt.%) versus Al_2O_3 (wt.%). (e) Fe_2O_3 (wt.%) versus Al_2O_3 (wt.%). (f) Fe/Al mass ratio (log scale) versus SiO_2 (wt.%). The dashed line and blue zone depict the average value and the range of Fe/Al mass ratio of shales deposited in oxic and suboxic environments ($\sim 0.53 \pm 0.11$; Raiswell et al., 2008; Taylor and McLennan, 1985; Lyons and Severmann, 2006).

Rasmussen et al., 2005). The quartz tubes were then sealed under vacuum and combusted at 950 °C for 6 h and 600 °C for another 2 h for separating N_2 from other volatiles (mainly CO_2 and H_2O). After combustion, the gas was extracted from the tube loaded in ultra-high vacuum line ($\sim 4 \times 10^{-9}$ mbar), purified and quantified with a capacitance manometer. Subsequent N isotope analyses were performed on a static mass spectrometer allowing measurement of nanomole quantities of N_2. The nitrogen blank amount and isotope composition of the sealed tubes were on average 2.63 ± 0.73 nmol and $3.59 \pm 1.80‰$ ($n = 9$), respectively. After blank correction, analysis of the internal standard 09–02 (Alpine metagabbro) gave a mean N content of 6.00 ± 0.81 ppm and $\delta^{15}N_{bulk}$ value of $8.23 \pm 0.41‰$, consistent with previously published values ($N = 4$ ppm, $\delta^{15}N_{bulk} = 8.1‰$; Busigny et al., 2005). The slight difference in N content relative to former measurements of this standard probably results from different degassing temperature of the sample (300 °C here *versus* 450 °C in our previous study; Busigny et al., 2005). All N content and $\delta^{15}N_{bulk}$ values presented in this paper were corrected for blank contribution. The isotope data are reported using the conventional δ notation (in permil) with respect to air standard, with $\delta\ ^{15}N_{bulk} = [(^{15}N/^{14}N)_{sample}/$

Table 2
Iron speciation of TCDP samples selected from T2 and T3 drill cores.

Sample	Rock Type	Depth* m	Fe_T %	Fe_{carb} %	Fe_{ox} %	Fe_{mag} %	Fe_{py} %	PRS %	Fe_{py}/Fe_{HR} ‰	Fe_{HR}/Fe_T ‰
Kazput Formation										
T3 76.24–76.33	Shale	76.30	4.99	0.47	0.09	0.19	0.06	0.69	0.08	0.16
T3 79.15	Shale	79.15	5.15	0.92	0.07	0.20	0.09	0.79	0.07	0.25
T3 86.28	Carbonate	86.28	3.09	0.48	0.04	0.08	0.06	0.39	0.09	0.22
T3 164.36–164.43	Shale	164.39	19.49	3.05	0.82	0.76	1.81	3.43	0.28	0.33
T3 174.22	Shale	174.22	9.63	1.09	0.17	0.26	0.27	3.64	0.15	0.19
Average									**0.13**	**0.23**
Meteorite Bore Member										
T2 194.04	Diamictite	194.04	4.58	0.58	0.22	0.20	0.21	0.89	0.18	0.26
T2 259.30	Diamictite	259.30	5.19	0.44	0.04	0.15	0.15	1.20	0.20	0.15
T2 283.90	Diamictite	283.90	5.52	1.10	0.29	0.50	0.19	0.86	0.09	0.37
Average									**0.16**	**0.26**
Kungarra Formation										
T2 298.00	Shale	298.00	5.96	0.35	0.08	0.31	0.12	1.18	0.14	0.14
T2 309.10	Shale	309.10	5.48	1.07	0.21	0.40	0.14	1.06	0.08	0.33
T2 312.39	Shale	312.39	6.06	0.63	0.25	0.34	0.20	0.86	0.14	0.23
T2 335.55	Shale	335.55	3.53	0.66	0.28	0.16	0.17	0.63	0.14	0.36
T2 347.45	Shale	347.45	6.03	0.64	0.25	0.26	0.10	0.65	0.08	0.21
T2 359.43–359.50	Shale	359.46	5.84	0.72	0.19	0.32	0.18	0.42	0.13	0.24
T2 363.90	Shale	363.90	4.64	0.84	0.22	0.22	0.20	0.59	0.14	0.32
Average									**0.12**	**0.26**

* Depth in T2 and T3 drill core recovered by the Turee Creek Drilling Project (TCDP).

$(^{15}N/^{14}N)_{Air} - 1] \times 1000$. The reproducibility on samples N_{bulk} content and $\delta\ ^{15}N_{bulk}$ values were always better than ± 0.5 ppm (1 σ) and ± 0.5‰ (1σ), respectively.

4. RESULTS

4.1. Major element concentrations and Fe speciation data

Major element concentrations in T2 and T3 samples are given in Table 1 and some general features are illustrated in Fig. 2. SiO_2 content shows a large range of variations from 5.20 to 81.08 wt.%, highly dependent on lithology, and averaging ~29.48 wt.% in carbonate, ~55.83 wt.% in shale, ~64.79 wt.% in diamictite and ~72.15 wt.% in quartzite and sandstone. Negative correlations are observed between CaO and SiO_2 contents (Fig. 2a), reflecting mixing between carbonates and various silicate minerals (quartz, chlorite, micas). The positive correlation between Al_2O_3 and SiO_2 (Fig. 2b) in T2 and T3 samples indicates that Al and Si are contained in layer silicates (chlorite, micas), expressing a progressive transition from carbonate-rich to shale-rich rocks. For SiO_2 content higher than ~56 wt.%, a negative trend defined by quartzite/sandstone indicates that SiO_2 increase is tied to the presence of quartz rather than layer-silicate minerals. Al_2O_3, K_2O and TiO_2 contents vary from 1.50 to 20.32 wt.%, 0.00 to 4.69 wt.%, and 0.04 to 0.83 wt.%, respectively. They are positively correlated to each other (Fig. 2c-d) and track the relative proportions of detrital component to the samples. It can be noted that Kazput carbonates define a better correlation than other geological units, which are more scattered (Fig. 2c-d).

Furthermore, total iron (Fe_T) content, expressed as Fe_2O_3, varies from 2.13 to 29.01 wt.% (average = 7.19 wt. %) and is linearly correlated to Al_2O_3 (Fig. 2e) for most samples. Fe_T/Al mass ratio (Fig. 2f) shows a stable value around 0.64 in most T2 and T3 samples, except four carbonates and shales from Kazput Formation, which have higher Fe/Al ratio (*i.e.* Fe-enrichment; Fig. 2e-f). The relatively constant Fe_T/Al ratio of most samples possibly reflects lithogenic contribution and is only slightly higher than the average value of shales deposited in oxic and suboxic environments (~0.53 ± 0.11; Taylor and McLennan, 1985; Lyons and Severmann, 2006; Raiswell et al., 2008). Moreover, Fe_T/Al ratio is sensitive to detrital mineralogy and sedimentation rates. In mafic or ultramafic settings, Fe_T/Al ratios of sediments can be quite high, even if the Fe is largely contained in silicates rather than authigenic minerals (*e.g.* Stüeken et al., 2017). Conversely, high sedimentation rates with minerals that have crustal Fe_T/Al ratios can dilute Fe enrichments (Lyons and Severmann, 2006). Accordingly, oxic conditions cannot be firmly established from Fe_T/Al ratios alone. Iron speciation data of shales selected to represent the different geological units were thus obtained to provide further constraints on the redox state of the paleo-water column in the Turee Creek basin (Table 2). Highly reactive iron (Fe_{HR}), which corresponds to Fe in carbonates, oxides, magnetite and pyrite, can be enriched in sediments deposited under anoxic conditions, either ferruginous or euxinic (*e.g.* Poulton and Canfield, 2005, 2011; Planavsky et al., 2011; Izon et al., 2017). A ratio Fe_{HR}/Fe_T higher than 0.38 indicates anoxic conditions while lower values point to oxic to suboxic conditions. In the present work, shales from Kungarra, Meteorite Bore Member and Kazput Formations show Fe_{HR}/Fe_T in the range 0.14–0.36 (average 0.26, n = 7), 0.15–0.37 (average 0.26, n = 3) and 0.16–0.33 (average 0.23,

n = 5), respectively, therefore supporting deposition under oxic to suboxic conditions for both T2 and T3 samples.

4.2. Carbon content and isotope composition

Depth profiles of organic C content (TOC) and $\delta^{13}C_{org}$ value in T2 and T3 samples are plotted in Fig. 3. Organic C content ranges from 62 to 1492 ppm (avg. 783 ± 332 ppm, n = 30) in T2 samples and from 67 to 1338 ppm (avg. 567 ± 307 ppm, n = 54) in T3 samples. Thus, there is no significant difference between the two drill cores. Organic C content seems to vary according to lithology, with shales being enriched in C_{org} compared to other sediments. In contrast, organic C isotope composition shows a marked distinction between T2 and T3, with average $\delta^{13}C_{org}$ values of −34.5 ± 1.7 ‰ (n = 30) and −28.3 ± 1.6 ‰ (n = 54), respectively. In detail, $\delta^{13}C_{org}$ values are also subtly controlled by lithology. In T2, $\delta^{13}C_{org}$ values decrease from Kungarra sandstone (avg. −30.6 ± 2.5 ‰, n = 3), Meteorite Bore Member diamictite (avg. −34.2 ± 0.8 ‰, n = 9), to Kungarra shale (avg. −35.2 ± 0.6 ‰, n = 18). In T3, $\delta^{13}C_{org}$ values increase from Kazput shale (avg. −29.6 ± 1.0 ‰, n = 25) to Kazput carbonate (avg. −27.0 ± 0.8 ‰, n = 27). Finally, $\delta^{13}C_{org}$ values show negative trends with TOC content (Fig. 4a), Al_2O_3 content (Fig. 4c) and molar C_{org}/N_{bulk} ratio (Fig. 4e).

4.3. Nitrogen content and isotope composition

Depth profiles of N_{bulk} content and $\delta^{15}N_{bulk}$ values in T2 and T3 samples are shown in Fig. 3. Bulk N content is low, and varies from 13.5 to 56.7 ppm (avg. 34.3 ± 12 ppm, n = 11), and 15.7 to 53.4 ppm (avg. 32.4 ± 11.9 ppm, n = 13) in T2 and T3 samples, respectively. Significant positive correlations are found between N_{bulk}

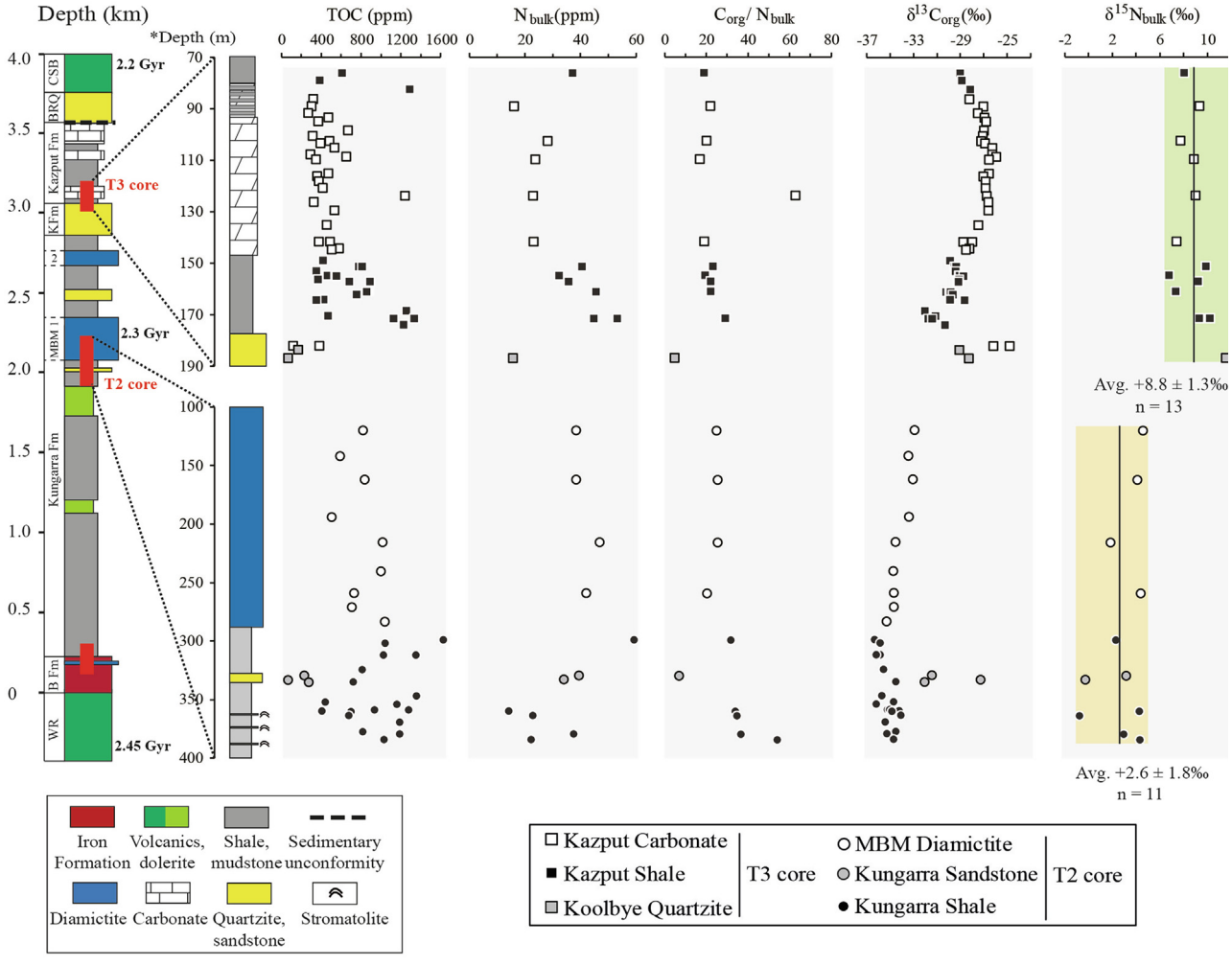


Fig. 3. Total organic carbon (TOC) and nitrogen contents (both in ppm), isotope compositions (‰), and C_{org}/N_{bulk} molar ratio of the Turee Creek samples (symbols as in Fig. 2). *Depth is the depth in the drill cores. The light green and orange bands represent the ranges of N isotope composition of T3 and T2 samples, respectively. WR, Woogarra rhyolites; B Fm, Boolgeeda Iron Formation; Kungarra Fm, Kungarra Formation; MBM, Meteorite Bore Member (including Member 1 and Member 2); K Fm, Koolbye Formation; Kazput Fm, Kazput Formation; BRQ, Beasley River Quartzite; CSB, Cheela Springs Basalt. (For interpretation of the references to colour in this figure legend, the reader is referred to the web version of this article.)

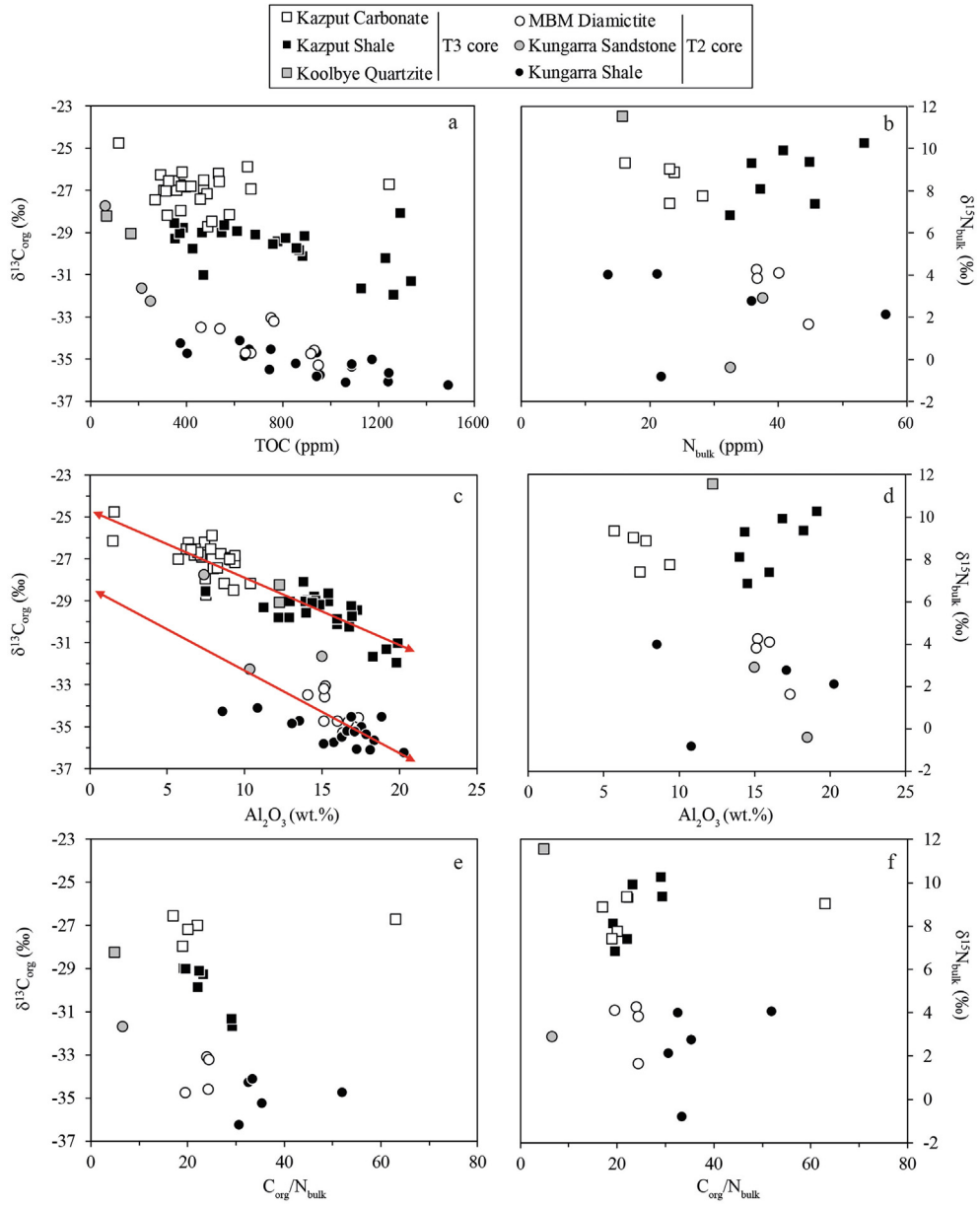


Fig. 4. Relations between organic C isotope composition (‰ vs PDB), TOC (ppm), bulk N isotope composition (‰ vs Air), N_{bulk} (ppm) and Al_2O_3 content (wt.%) in the Turee Creek samples. (a) Organic C isotope composition (‰ vs PDB) versus TOC (ppm). (b) Bulk N isotope composition (‰ vs Air) versus N_{bulk} (ppm). (c) Organic C isotope composition (‰ vs PDB) versus Al_2O_3 content (wt.%). The two red lines represent a mixing between purported authigenic and detrital endmembers. (d) Bulk N isotope composition (‰ vs Air) versus Al_2O_3 content (wt.%). (e) Organic C isotope composition (‰ vs PDB) versus C_{org}/N_{bulk} molar ratio. (f) Bulk N isotope composition (‰ vs Air) versus C_{org}/N_{bulk} molar ratio. MBM, Meteorite Bore Member. (For interpretation of the references to colour in this figure legend, the reader is referred to the web version of this article.)

and TOC (Fig. 5a), K_2O (Fig. 5b) as well as Al_2O_3 content (Fig. 5c) in T2 and T3 samples.

The C_{org}/N_{bulk} molar ratio (avg. 25.9 ± 12.5, $n = 23$; Fig. 3) is low in comparison with other older or contemporary sedimentary rocks (C/N >> 100; *e.g.* Garvin et al., 2009; Thomazo et al, 2011; Luo et al., 2018). It does not display any correlation with either K_2O content (Fig. 5d), TOC or Al_2O_3 content (not shown).

Nitrogen isotope compositions show a bimodal distribution in T2 and T3 (Fig. 3), with $\delta^{15}N_{bulk}$ values from −0.8 to +4.3‰ (avg. $+2.6 \pm 1.8$‰, $n = 11$) and +6.8 to +11.5‰ (avg. $+ 8.8 \pm 1.3$‰, $n = 13$), respectively. These $\delta^{15}N_{bulk}$ differences do not correlate with N_{bulk} content (Fig. 4b), Al_2O_3 content (Fig. 4d) or molar C_{org}/N_{bulk} ratio (Fig. 4f). Additionally, in contrast to $\delta^{13}C_{org}$ values, $\delta^{15}N_{bulk}$ values do not show any correlation with lithological

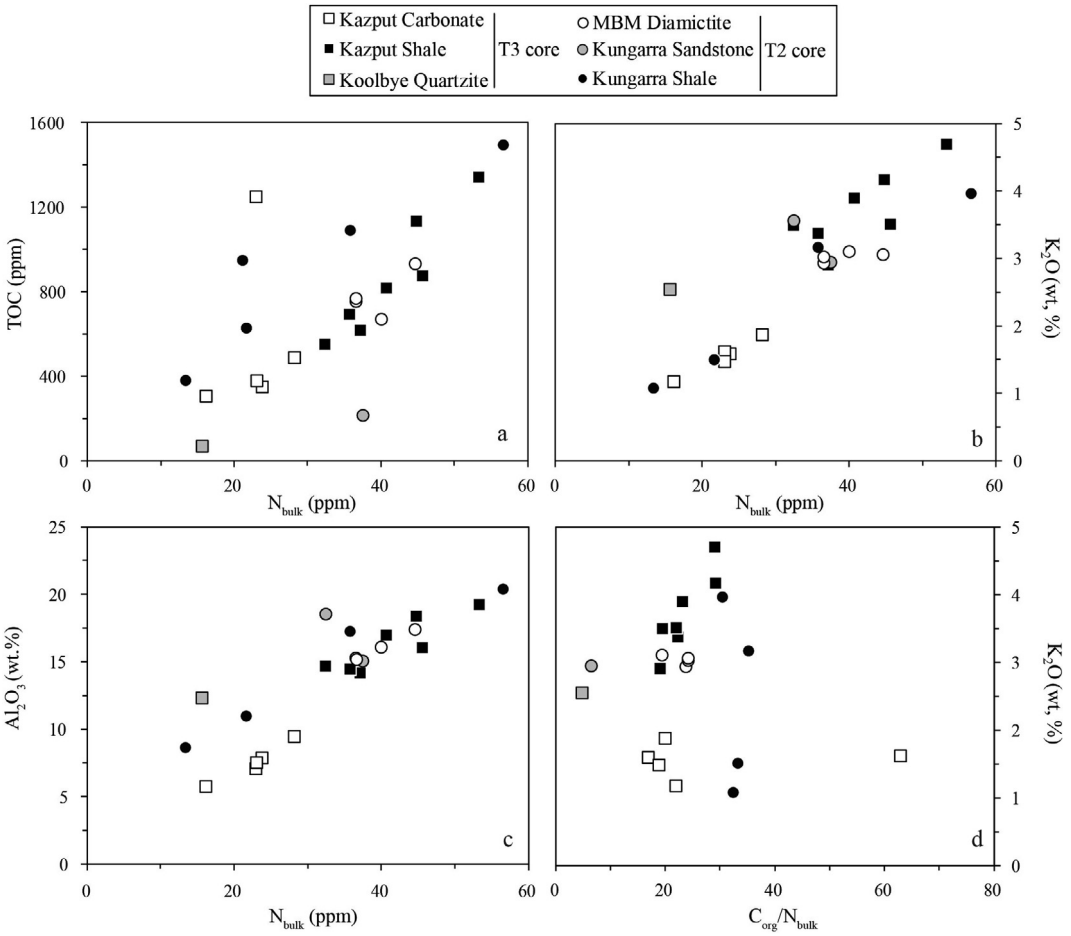


Fig. 5. Relations between TOC (ppm), N_{bulk} (ppm), K_2O content (wt.%), Al_2O_3 content (wt.%) and C_{org}/N_{bulk} molar ratio in the Turee Creek samples. (a) TOC (ppm) versus N_{bulk} (ppm). (b) K_2O content (wt.%) versus N_{bulk} (ppm). (c) Al_2O_3 content (wt.%) versus N_{bulk} (ppm). (d) K_2O content (wt.%) versus C_{org}/N_{bulk} molar ratio.

changes (*i.e.* carbonate, shale, diamictite, quartzite and sandstone).

5. DISCUSSION

5.1. Evaluation of the influence of modern organic matter contamination

Because of the low TOC and N contents in most samples from T2 and T3 (down to ~60 ppm TOC and 13.5 ppm N), it is primordial to evaluate potential contamination by modern organic matter. For instance, a recent experimental study determined that cleaning samples with organic solvents for removing modern organic matter can induce more contamination (*e.g.* up to 6000 ppm by cleaning with dichloromethane) and produce a bias on TOC and $\delta^{13}C$ measurements (homogeneous $\delta^{13}C$ between −27 and −29‰; Muller et al., 2018). The use of such solvent has thus been avoided in the present work and sample surface was cleaned only with mQ water (see section 3). Moreover, an organic contamination would be characterized by unique and homogeneous $\delta^{13}C$ and $\delta^{15}N$ values, which is not the case in the Turee Creek samples. For carbon, a contamination should have produced well-defined trends between $\delta^{13}C$ and TOC towards a specific $\delta^{13}C$ value (that of the contaminant). In contrast, samples from T2 and T3 with the lowest TOC contents show a wide range of $\delta^{13}C$ (Fig. 4a), as for instance samples T3-186.98 and T3-182.25 with values of −28.3 and −24.8‰, respectively (Table 2). Moreover, in the case of an organic contamination, the correlation observed between $\delta^{13}C$ and TOC should be better than the one between $\delta^{13}C$ and Al_2O_3, which is not the case (Fig. 4a and c). Finally, the blanks of CO_2 obtained in EA-IRMS measurements on empty tin capsules and on pure quartz powders were always lower than 0.1 μmol and represented less than 3% of the total CO_2 extracted from the samples.

For nitrogen, samples were degassed under vacuum at 300 °C overnight before N extraction thus excluding any contribution from N_2 adsorbed on the powder (*e.g.* air) and modern organic contamination. Additionally, if contaminated, samples with the lowest N content should show a $\delta^{15}N$ value specific of the contaminant. In contrast, N isotope compositions in T2 and T3 are not related to N concentrations (Fig. 4b) but are controlled only by stratigraphic positions of the samples, with $\delta^{15}N$ values around

+2.6 ± 1.8‰ in T2 and +8.8 ± 1.3‰ in T3 (Fig. 3). These different observations together with the strong stratigraphic control of C and N isotope compositions (Fig. 3) point to pristine/indigenous isotope signatures rather than secondary contamination.

5.2. Nitrogen speciation and isotope signature preservation in Turee Creek sediments

Before using N isotope composition as a tracer of paleoenvironmental conditions, the potential effects of diagenesis and metamorphism on N content and isotope signature need to be evaluated (*e.g.* Papineau et al., 2009; Busigny et al., 2013; Stüeken et al., 2015a; Ader et al., 2016). The correlations between N_{bulk} and TOC (Fig. 5a) as well as K_2O content (Fig. 5b) in T2 and T3 drill cores indicate that N in Turee Creek sediments is related to organic matter and K-bearing clay minerals. Basically, sedimentary N is derived from organic matter, and part of the organic N is released and replaces K in clay minerals during post-depositional processes, such as diagenesis and metamorphism. Combined with the correlations between N_{bulk}, TOC and K_2O contents, the relatively low C_{org}/N_{bulk} ratios (avg. = 25.9 ± 12.5) suggest that most of the organic N was preserved and replaced K^+ as inorganic NH_4^+-N in clay minerals, due to their similar charge and ionic radius (Honma and Itihara, 1981; Rouchon et al., 2005). An important concern is the possibility of a later modification by exogenous NH_4^+-containing fluid because N contents of the Turee Creek sediments are low. Assuming exogeneous NH_4^+ was added after sediment deposition, the rocks with more clay minerals should have fixed more NH_4^+, resulting in lower C_{org}/N_{bulk} ratios, in particular for the low TOC contents in T2 and T3 samples. Thus, negative correlations between K_2O or Al_2O_3 contents and C_{org}/N_{bulk} ratios should have been observed, which is not the case (Fig. 5d). Moreover, if part of the N would be derived from exogenous NH_4^+ with a specific N isotope signature, one would expect a correlation between K_2O or Al_2O_3 and $\delta^{15}N$, which again is not seen (Fig. 4d). A potential modification by exogeneous NH_4^+ cannot be deduced from the relations between TOC and N_{bulk} concentrations because different slops likely record various input of detrital organic matter (see below). We therefore conclude that N in Turee Creek sediments originated from organic matter and was transferred without significant isotopic fractionation as inorganic NH_4^+ in clay minerals in good agreement with previous studies of diagenetic effects in anoxic conditions (see review in Robinson et al., 2012), and on other Archean sedimentary sequences (*e.g.* Garvin et al., 2009; Stüeken et al., 2015a; Zerkle et al., 2017). The lower C_{org}/N_{bulk} ratios found here relative to previous studies are interpreted as exceptional N preservation because Al_2O_3 concentrations are highly enriched relative to TOC, and the diagenetic N-fixation into clay is thus stronger than in other geological formations. The Koolbye quartzite (T3) and Kungarra sandstone (T2) with the highest Al_2O_3/TOC ratio (average ~ 972) and lowest C_{org}/N_{bulk} ratio (average ~ 5.8) likely preserved most N while losing C during organic matter degradation, producing C/N slightly lower than the Redfield ratio (*i.e.* 6.6). In contrast, carbonates and shales with relatively lower Al_2O_3/TOC ratio (average ~ 206) and higher C_{org}/N_{bulk} ratio (average ~ 27.8) have probably lost part of their N and/or merely contain more N-poor detrital organic matter.

The absence of correlation between $\delta^{15}N_{bulk}$ and N_{bulk} content (Fig. 4b) or molar C_{org}/N_{bulk} ratio (Fig. 4f) in Turee Creek sediments also indicates no or minimal effect of diagenesis and metamorphism on N isotope composition. Therefore, the distinct N isotope compositions recorded in T2 and T3 samples (Fig. 3) must be explained by other factors than diagenesis or metamorphism. A lithological control can also be ruled out since T2 and T3 show a range of chemical composition and sediment types largely overlapping (Fig. 2).

5.3. Origin of the relation between C isotope composition of organic matter and Al concentration

The inverse correlation observed between $\delta^{13}C_{org}$ values and Al concentrations is an important feature of the present data set (Fig. 4c) and may arise from three different processes: (1) a preservation effect of organic matter, (2) a basinal redox gradient and/or (3) a mixing between authigenic and detrital organic matter (*e.g.* detrital graphite particles in Cryogenian Nantuo Formation of South China; Ye et al., 2019). These three possibilities are explored below.

First, in modern marine sediments, it is well known that deep shaly facies better preserve organic matter than more shallow facies such as, for instance, carbonates and sandstones (*e.g.* Hedges and Keil, 1995; Playter et al., 2017). This is mainly due to the low permeability of clay layers that prevent oxygenation of the shaly sediment, therefore limiting oxic degradation of organic matter. In contrast, carbonates and sandstones are more permeable and lose most of their organic matter when O_2-rich seawater diffuses into sediments porosity. Although this scenario could link Al_2O_3 (*i.e.* shale dependent) to TOC concentrations in theory, this should not produce a correlation with $\delta^{13}C_{org}$. We thus consider that this possibility is unlikely in the case of the Turee Creek sediments. Additionally, a limited amount of O_2 possibly available in bottom seawater of the basin would have prevented significant O_2 diffusion within any sediment.

Second, a redox and chemical gradient in the Turee Creek basin could potentially have impacted the C isotope composition of organic matter and be indirectly related to the proportion of clay particles deposited in the sediment. Several authors already invoked intra-basinal variations to explain $\delta^{13}C_{org}$ distribution in shallow- and deep-facies sediments from the Proterozoic (*e.g.* Bekker et al., 2008; Stüeken, 2013; Gilleaudeau and Kah, 2013; Guo et al., 2013; Luo et al., 2014). Carbon isotope compositions of shallow-facies sediments generally have $\delta^{13}C_{org}$ values of −25 to −27‰ and are attributed to photoautotrophic organisms. In contrast, deep-facies sediments with $\delta^{13}C_{org} < -30$‰ are interpreted as reflecting heterotrophs and/or chemotrophs thriving at or below a redoxcline (Bekker et al., 2008; Guo et al., 2013; Luo et al., 2014). In the case of the Turee Creek samples, such a scenario is

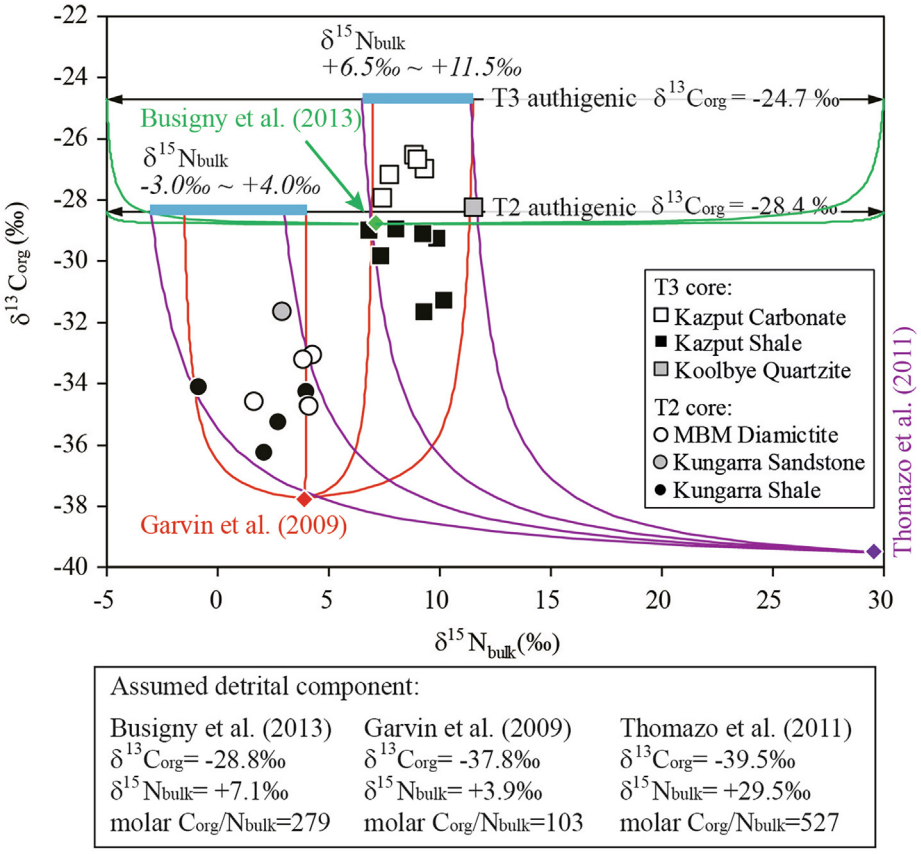


Fig. 6. Relation between organic C isotope composition (‰ vs PDB) and bulk N isotope composition (‰ vs Air). The curves represent mixing lines modeled between purported authigenic and detrital organic matter. The black lines with arrows correspond to authigenic $\delta^{13}C_{org}$ value (‰ vs PDB) determined from the relations between $\delta\ ^{13}C_{org}$ and Al_2O_3 (see details in the main text). The diamonds represent assumed detrital organic matter, for which the average values of $\delta^{15}N_{bulk}$, $\delta^{13}C_{org}$ and C_{org}/N_{bulk} molar ratio are taken from samples older than 2.45 Ga (data from Garvin et al., 2009; Thomazo et al., 2011; Busigny et al., 2013). The blue bands represent the possible range of authigenic $\delta^{15}N_{bulk}$ values (‰ vs Air; values in italic) deduced from modeling for T2 and T3 samples. (For interpretation of the references to colour in this figure legend, the reader is referred to the web version of this article.)

compatible with lithological variations since deep-facies shales show more negative $\delta\ ^{13}C_{org}$ values than shallow-facies sandstones and carbonates (Fig. 3). In parallel, Al concentrations would be higher in deep sediments due to a larger proportion of detrital clay particles. In this scenario, N isotope composition could eventually track changes in the local biomass added to the sediment and thus follows $\delta\ ^{13}C_{org}$ values, in particular if the N source used by living organisms is affected by chemical reactions at a redoxcline. In contrast, $\delta\ ^{15}N$ values are decoupled from $\delta\ ^{13}C_{org}$ and show a bimodal distribution in T3 and T2, independent of lithological variations (Fig. 3). Notably, the Kazput Formation contains deep-facies shales with $\delta\ ^{15}N$ values undistinguishable from associated shallow-water carbonates (Fig. 3). Finally, Fe_T/Al ratios and Fe mineral speciation data of shales do not show evidence for anoxic conditions in any of the samples analyzed herein. Taken together, these observations are not supportive of intra-basinal redox variability but we cannot exclude subtle redox variations for instance from oxic to suboxic conditions, which may not be identified from Fe mineral speciation.

A third and last hypothesis for explaining the correlation between $\delta^{13}C_{org}$ and Al concentration is a mixing between authigenic and detrital particles. More specifically, the negative correlation between $\delta^{13}C_{org}$ and Al_2O_3 content suggests that ^{13}C-depleted organic matter (OM) was eventually inherited from detrital input. Conversely, the ^{13}C-enriched OM would represent primary export production with typical photosynthetic $\delta^{13}C_{org}$ values (Schidlowski, 2001). As shown in Fig. 4c, the $\delta^{13}C_{org}$ signatures of primary photosynthetic OM in T2 and T3 can be extrapolated at −24.7‰ and −28.4‰, respectively, assuming that the authigenic endmember is devoid of aluminum (*i.e.* $Al_2O_3 = 0$ wt.%). It can be noted that the authigenic endmember may contain some Al_2O_3, for instance if adsorption of biomass onto clay minerals is an important preservation mechanism for organic carbon (and nitrogen). In that case, the calculated $\delta\ ^{13}C$ endmembers would represent extreme scenarios. The two distinct $\delta^{13}C_{org}$ values of authigenic endmembers estimated from T2 and T3 samples (Fig. 3) possibly reflect different isotope effects associated with photosynthesis, which is known to depend on modifi-

cations in the type and/or size of living organisms, and/or environmental factors such as temperature (Mook et al., 1974) and the partial pressure of atmospheric CO_2 (*e.g.* Popp et al., 1998; Hayes et al., 1999; Sansjofre et al., 2011).

Assuming that detrital organic matter was deposited in Turee Creek sediments, it is important to estimate its potential impact on N isotope composition, which has been found significant in other formations (Ishida et al., 2017). Contrasting with organic carbon, N isotope compositions do not display any relationship with Al_2O_3 content, suggesting that possible detrital OM input has no or very little effect on $\delta\,^{15}N_{bulk}$ values. The decoupling between C and N isotope compositions in Turee Creek sediments can be interpreted as resulting from a high flux of detrital organic C, but a low detrital N flux. This would correspond to a detrital organic material with high C/N ratio. Interestingly, in the Hamersley Basin, Western Australia, sedimentary sequences older than the Turee Creek Group are all characterized by high C/N ratio, with values up to 1719 in the 2.7 Ga old Tumbiana Formation (Garvin et al., 2009; Thomazo et al., 2011; Busigny et al., 2013; Stüeken et al., 2015b) and low $\delta^{13}C_{org}$ values (*e.g.* average of ~−37.8‰ and −39.5‰ in Mount McRae Shales and Tumbiana formations). These older sediments of the Hamersley and Fortescue groups with high C/N molar ratio and low $\delta^{13}C_{org}$ could represent potential sources of detrital OM to the Turee Creek sediments. A detrital origin of organic C from sediments of the Hamersley Basin is supported by recent U-Pb-Hf isotope systematics of more than 1500 detrital zircons extracted from the same core samples than the one analyzed in this study. Specifically, Caquineau et al. (2018), showed that the vast majority of T1 and T2 zircons show a range of age distribution with three major peaks at 2.45, 2.52, and 2.68 Ga, which are consistent with those of the underlying 2.45–2.78 Ga Hamersley and Fortescue groups. More recently, Caquineau et al. (in review) analyzed the same zircons for their Hf isotopic compositions and showed that they are significantly different from zircon Hf isotope data of the nearby Glenburgh Terrane, located to the south of the Turee Creek Group, or older successions of the Pilbara or Kaapvaal cratons. This together with U-Pb age constraints have led these authors to propose that the main source of Turee Creek zircons was the underlying subaerial volcanic sequences of the Hamersley and Fortescue groups, which are interleaved with the sedimentary successions displaying the high C/N ratio and low $\delta^{13}C_{org}$ values. Erosion of both the subaerial basalts and associated sedimentary successions could account for the dominant zircon population and specific flux of detrital organic C (high C/N ratio and low $\delta^{13}C_{org}$ values) to the Turee Creek basin. In addition, some of these older sediments have extremely positive $\delta\,^{15}N$ values (Thomazo et al., 2011; Stüeken et al., 2015b) and could have impacted the N isotope signature of the Ture Creek sediments, possibly explaining high $\delta\,^{15}N_{bulk}$ values in T3 samples (Fig. 3). In the following, we thus modelled the contribution of such a detrital N input to the Turre Creek sediments in order to estimate the primary authigenic N isotope signatures and reconstruct the paleo-environment and -ecosystem.

In the model, the three sedimentary sequences older than the Turee Creek Group and analyzed in previous studies for C and N isotope compositions were used as potential detrital OM sources (Fig. 6). These sequences are the 2.7 Ga Tumbiana Formation (Thomazo et al., 2011; Stüeken et al., 2015b), the 2.5 Ga Mount McRae Shales (Garvin et al., 2009), and the 2.45 Ga Brockman Iron Formation (Busigny et al., 2013). Each sedimentary sequence was considered independently from the others, so that three different mixing relationships were built in the model. The endmembers used as detrital component correspond to the average values of $\delta\,^{13}C_{org}$, $\delta\,^{15}N_{bulk}$ and C_{org}/N_{bulk} molar ratio for each sedimentary sequence (Fig. 6). In the model, $\delta\,^{13}C_{org}$ value and C_{org}/N_{bulk} molar ratio of authigenic endmembers were fixed at −24.7 and −28.4‰, and 6.6 and 5.0 for T2 and T3, respectively (as deduced from the trends observed in Fig. 4c and the minimum C/N values in Fig. 4e). The results of the mixing model show that detrital endmembers from Mount McRae Shales (Garvin et al., 2009) and Tumbiana Formation (Thomazo et al., 2011; Stüeken et al., 2015b) can reproduce the range of $\delta^{13}C_{org}$ and $\delta\,^{15}N_{bulk}$ values measured in the Turee Creek sediments (Fig. 6). In contrast, sedimentary rocks from the Brockman Iron Formation (Busigny et al., 2013) are unlikely detrital endmembers for the Turee Creek sediments. Therefore, the N isotope signatures of primary authigenic organic matter were determined by considering only Mount McRae Shales and Tumbiana Formation as possible detrital sources. The calculated $\delta\,^{15}N$ values of authigenic components are comprised between −3 to +4‰ (avg. = +1.5‰) for T2, and +6.5 to +11.5‰ (avg. = +8.6‰) for T3 (Fig. 6). These results are close to raw $\delta\,^{15}N$ values measured in bulk sediments (+2.6‰ in T2 and +8.8‰ in T3; Fig. 3), thus confirming a small effect of detrital organic matter input on N isotope composition of the Turee Creek sediments. Although this finding may be surprising when considering extreme $\delta\,^{15}N_{bulk}$ values of the Tumbiana Formation (~+30‰; Thomazo et al., 2011; Stüeken et al., 2015b), this reflects that detrital organic matter was characterized by particularly elevated C/N ratio, and thus low N content (bulk rock N concentration in Tumbiana averages 4.7 ± 3 ppm, which is one order of magnitude lower than in Turee Creek; Thomazo et al., 2011; Stüeken et al., 2015b). Overall, we conclude that the large difference in $\delta\,^{15}N_{bulk}$ values recorded in T2 and T3 sediments was caused by changes of paleo-environmental conditions rather than variable detrital N sources. Thus, $\delta\,^{15}N_{bulk}$ values in Turee Creek sediments likely reflect N isotope composition of ~2.31 Ga primary producers thriving in the water column.

5.4. Implications for paleo-environment and -ecosystem

The N isotope signature of the Turee Creek sediments can be used to constrain paleo-environment and -ecosystem during the Great Oxidation Event. The most striking feature observed in the present data is the rise in $\delta\,^{15}N$ values from about +1.5 ± 1.9‰ in T2 to +8.6 ± 1.4‰ in T3 samples after correcting for minor detrital effect. This rise is independent from lithological variations

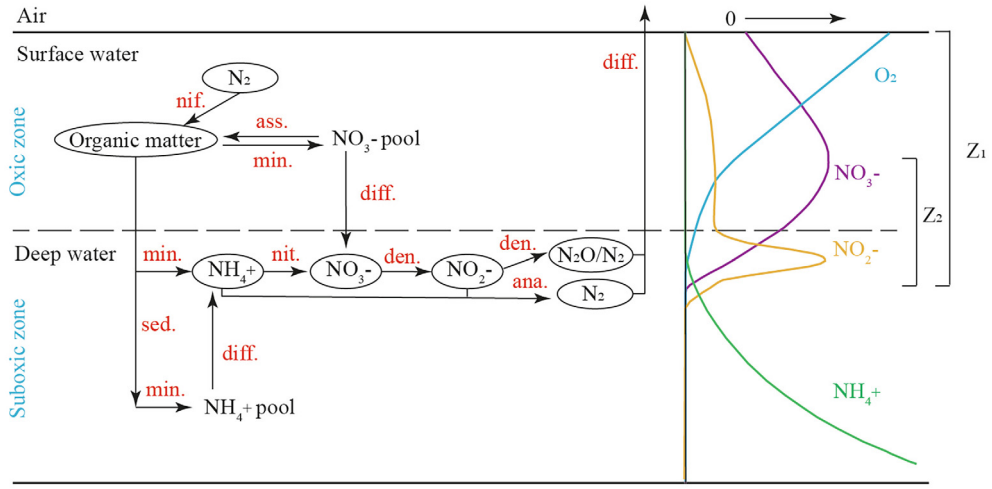


Fig. 7. Schematic representation of the biogeochemical nitrogen cycle used for modeling Turee Creek marine basin. nif., nitrogen fixation; ass., assimilation; min., mineralization; diff., diffusion; nit., nitrification; den., denitrification; ana., anammox. The colored curves represent the profiles of dissolved O_2, NO_3^-, NO_2^- and NH_4^+ concentrations in the water column. Z_1, distance between the depth of maximum O_2 concentration and the depth where oxygen concentration is zero; Z_2, distance between the depth of maximum NO_3^- concentration and the depth where NO_3^- concentration is zero. The dashed line represents the redox boundary of oxic and suboxic water.

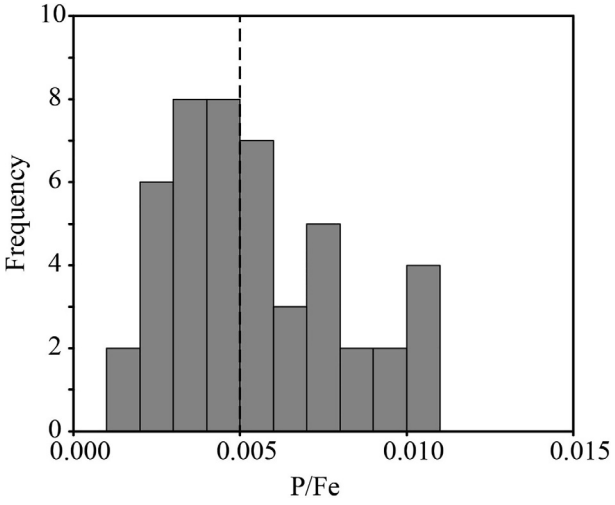


Fig. 8. Distribution of P/Fe molar ratio in Banded Iron Formations from Boolgeeda (samples from T1 drill core, see in Fig. 1 for drill location). The dash line indicates the average P/Fe (0.0050 ± 0.0026, 1 σ, n = 47).

in T2 and T3, and thus likely indicates a change in the N biogeochemical cycle in the Turee Creek basin. Increase of $\delta^{15}N$ value in sedimentary rocks is generally interpreted as resulting from isotope fractionation during fixed-N loss from the ocean water column (*e.g.* Beaumont and Robert, 1999; Garvin et al., 2009; Godfrey and Falkowski, 2009; Thomazo et al., 2011; Stüeken et al., 2013; Ader et al., 2016; Zerkle et al., 2017; Kipp et al., 2018). Four mechanisms were invoked to induce a loss of the fixed-N pool under either anoxic or oxic conditions in the Precambrian. Under dominantly anoxic conditions, ammonium (NH_4^+) is the main dissolved N species in the ocean. The pool of NH_4^+ can be depleted by (1) a loss of gaseous NH_3 under high pH (>9), producing a shift from NH_4^+ to NH_3 and associated NH_3 volatilization (Wada and Hattori, 1990; Li et al., 2012; Stüeken et al., 2015b), (2) partial oxidation of ammonium, followed by complete denitrification of any produced nitrite and nitrate (Thomazo et al., 2011), and/or (3) partial ammonium assimilation by the biomass (Papineau et al., 2009). Under oxic conditions, the main dissolved N species is nitrate (NO_3^-), like in the modern ocean. The pool of NO_3^- can be depleted by (4) partial denitrification and/or anammox (*i.e.*, anaerobic ammonium oxidation) under suboxic to anoxic conditions (Garvin et al., 2009; Godfrey and Falkowski, 2009; Zerkle et al., 2017; Luo et al., 2018; Kipp et al., 2018). Although the magnitude of N isotope fractionation varies between the four mechanisms presented above, all of them are associated with a preferential loss of light isotope from the ocean, resulting in heavy residual fixed-N pool (NH_4^+ or NO_3^-, then assimilated by living organisms; see discussion in Busigny et al., 2013). In the Turee Creek depositional environment, anoxic conditions seem unlikely because Fe/Al ratio is similar to the average ratio of shales deposited in oxic and suboxic environments (Taylor and McLennan, 1985; Lyons and Severmann, 2006; Raiswell et al., 2008; Fig. 2f). Furthermore, Fe mineral speciation data from the different units in T2 and T3 show Fe_{HR}/Fe_T ratio lower than 0.38, confirming oxic to suboxic conditions (*e.g.* Poulton and Canfield, 2005, 2011; Planavsky et al., 2011). These results imply that the mechanisms (1) to (3) should be discarded. Free O_2 was likely present in Turee Creek seawater, promoting an aerobic N cycle, associated with isotope fractionations such as those of mechanism (4).

In detail, the N biogeochemical cycle in the Turee Creek basin may have been as follows. Nitrogen was mostly introduced into the ocean by N_2-fixing microorganisms, such as cyanobacteria. The nitrogen isotope composition of these organisms is usually close to 0‰ (*e.g.* Minagawa and

Table 3
Parameters used for the calculation of dissolved nitrate and oxygen concentrations.

Parameter	Definition	Value	Reference
$R_{N:P}$	Redfield ratio of nitrogen and phosphorus	16	Gruber and Deutsch (2014)
K_{ads}	Adsorption constant of phosphorus on iron oxides	0.048–0.139 μM^{-1}	Jones et al. (2014)
Fe^{3+}/Fe_{tot}	Statistic ratio of ferric Fe and total Fe in Archaean and Proterozoic BIFs	0.43	Bjerrum and Canfield (2002)
P_{ads}/Fe_{tot}	Molar ratio of phosphorus and total Fe in T1 core	0.005	This study, see Fig. 8
D_{O2}	Diffusion coefficient of oxygen in seawater at 0 °C	1.2E-5 cm^2s^{-1}	Broecker and Peng (1974)
D_{O2}	Diffusion coefficient of oxygen in seawater at 24 °C	2.3E-5 cm^2s^{-1}	Broecker and Peng (1974)
D_{NO3}	Diffusion coefficient of nitrate in seawater at 0 °C	9.5E-6 cm^2s^{-1}	Chang and Devol (2009)
D_{NO3}	Diffusion coefficient of nitrate in seawater at 24 °C	1.9E-5 cm^2s^{-1}	Chang and Devol (2009)
$R_{O2:NO3}$	Consumed oxygen per molar nitrate produced	8.625	Redfield et al. (1963)

Wada, 1986), but may have reached negative $\delta^{15}N$ values (down to −7‰) depending on the type of metal cofactor used for N_2-fixation (Zerkle et al., 2008; Zhang et al., 2014). Mineralization of these organisms in the water column or sediments releases ammonium (NH_4^+) without fractionation, which in the presence of free O_2, was readily oxidized to NO_3^-. In O_2-depleted environments, such as oxygen-minimum zones, NO_3^- dissolved in the water column was partially reduced by denitrification or anammox into gaseous N_2 or N_2O (Lam and Kuypers, 2011). During denitrification and anammox, ^{14}N is preferentially released relative to ^{15}N, leaving the residual marine NO_3^- enriched in heavy isotope (average marine $\delta^{15}N_{NO3-}$ ~+5‰; Brandes and Devol, 2002). The heavy isotope signature of residual NO_3^- was transferred by assimilation to organisms living in the water column and finally recorded in sedimentary organic matter. Accordingly, assuming a steady-state system, the N isotope composition of organic matter in oxic marine environment should reflect mainly the relative proportion of partial N denitrification *versus* N_2-fixation. The extremely low TOC content of the Turee Creek sediments relative to contemporaneous sediments (*e.g.* ~2.31 Ga old sediments from Rooihoogte and Timeball Hill formations, South Africa; Zerkle et al., 2017; Luo et al., 2018) implies that primary productivity was low, remineralization was very efficient and/or sediment depositional rate was high. Low primary productivity and high remineralization could have resulted from limited nutrient availability and relatively high O_2 content in the water column, respectively.

In the framework of Fe speciation evidence for oxic or suboxic conditions, the marked increase in primary N isotope composition between T2 ($\delta^{15}N_{bulk}$ ~ −3‰ to +4‰, avg. +1.5‰) and T3 ($\delta^{15}N_{bulk}$ ~ +6.5‰ to +11.5‰, avg. +8.6‰) sediments can be interpreted as a stepwise increase of dissolved O_2 level during the Great Oxidation Event. Previous studies developed a conceptual model to predict how sedimentary $\delta^{15}N$ signature would vary as dissolved O_2 concentration increases in deep seawater (Fennel, 2005; Quan et al., 2008; Luo et al., 2018; Kipp et al., 2018). When there is hardly any O_2 in the water column, sedimentary $\delta^{15}N$ value is close to 0‰, *i.e.* N_2 fixation signature. Any NO_3^- production is nearly quantitatively denitrified so that N_2 fixation dominates and $\delta^{15}N$ remains near 0‰. As O_2 level rises, beyond a "tipping point", denitrification is no more quantitative, and residual nitrate with positive $\delta^{15}N$ values can accumulate. Finally, when dissolved O_2 concentration further increases and pushes the redox-boundary deeper, partial denitrification in the water column is inhibited. Denitrification is restricted to the pore waters where it is quantitative, so that the $\delta^{15}N$ value decreases again towards 0‰. The low primary $\delta^{15}N$ values observed in T2 (~+1.5‰) most likely reflect a biomass dominated by N_2-fixation in a dominantly suboxic water column where nitrate is nearly quantitatively denitrified, which limits the denitrification isotopic signal. In contrast, the higher primary $\delta^{15}N$ values of T3 (~+8.6‰) would point to an increasing NO_3^- availability due to lower rate of denitrification compared to nitrification. The limited $\delta^{15}N$ variability observed in T3 suggests a relatively stable pool of dissolved nitrate. On the time scale represented by the samples of each core (one to several tens of millions of years; Philippot et al., 2018), the N isotope cycling of the Turee Creek basin seems to be near-steady state regime. This suggests a significant increase of NO_3^-, and thus accumulation of O_2 between T2 and T3 sediment deposition, with relatively rapid change of the water column redox state, in good agreement with recent studies focused on the GOE (*e.g.* Luo et al., 2016, 2018; Zerkle et al., 2017; Kipp et al., 2018). Interestingly, a detailed study of the 2.31 Ga Rooihoogte and Timeball Hill formations in South Africa concluded to a similar timing for the transition from O_2-poor environment, with near quantitative nitrification and denitrification (N_2 fixation being the main source for biological N), to O_2-excess environment where NO_3^- was available (Luo et al., 2018). This supports large-scale ocean oxygenation at least in shallow waters, even if anoxic environment may have been preserved in deep waters.

5.5. Modeling dissolved nitrate and oxygen concentrations in the Turee Creek basin

In this section, we use a simple model, modified from previous studies (Voss et al., 2001; Fennel, 2005), to estimate the concentrations of dissolved NO_3^- and O_2 in Turee Creek basin waters (Figs. 7 and 8). As mentioned above, the N isotope biogeochemical cycle of the Turee Creek basin is assumed to be near steady state, where NO_3^- is present in shallow waters and can be assimilated by biomass (Fig. 7). In suboxic zone such as oxygen minimum zone in the water column or near sediment-water interface,

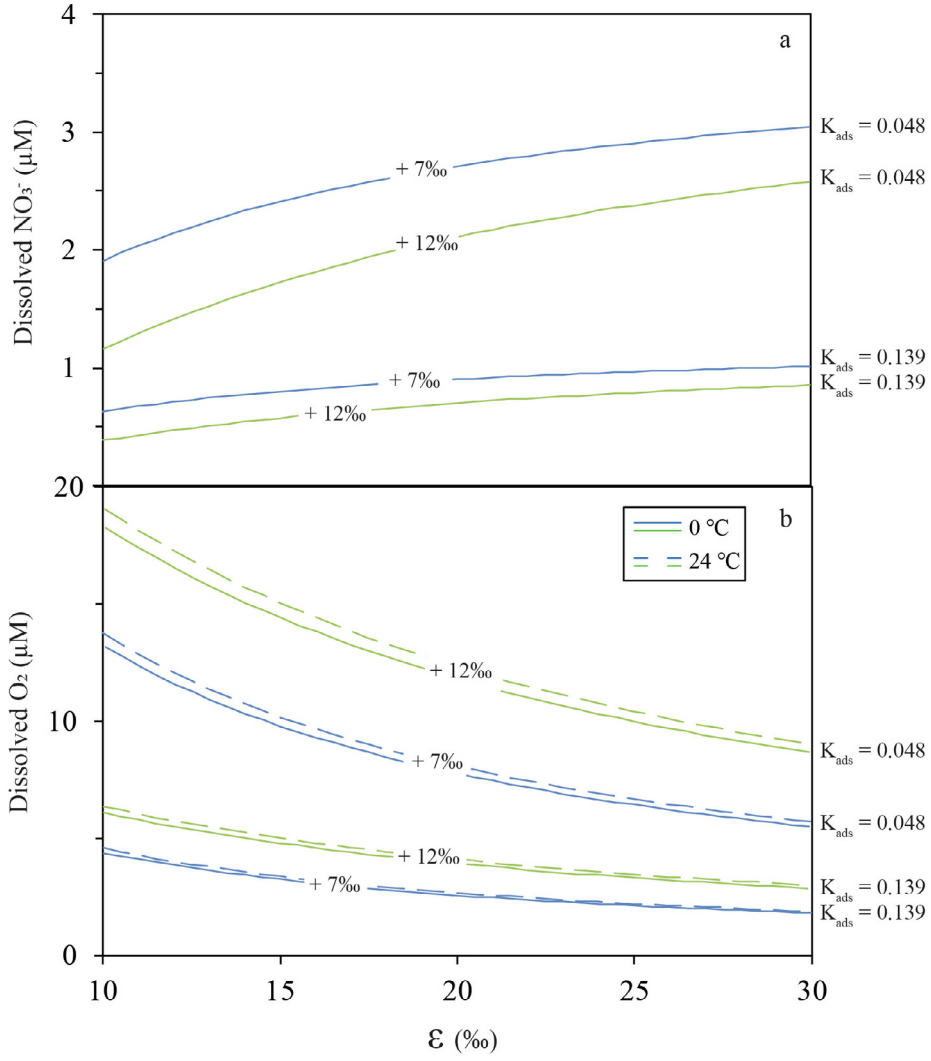


Fig. 9. Calculated results of dissolved nitrate and oxygen concentrations in seawater during T3 deposition. (a) Dissolved nitrate concentration versus N isotope enrichment factor (ε). (b) Dissolved oxygen concentration versus N isotope enrichment factor (ε). Blue and green curves indicate the calculated dissolved nitrate (a) and oxygen (b) concentrations when dissolved nitrate has a N isotopic composition of +7‰ ($f_{\text{nitrate-using organisms}} = 1$; the fraction of nitrate-using organisms in sedimentary organic matter) and +12‰ ($f_{\text{nitrate-using organisms}} \approx 0.6$), respectively. The solid lines and dashed lines in (b) are calculated dissolved O_2 concentrations based on diffusion coefficients at temperatures of 0 and 24 °C in surface water, respectively. (For interpretation of the references to colour in this figure legend, the reader is referred to the web version of this article.)

NO_3^- is converted to NO_2^- (Fig. 7), which is subsequently transformed to gaseous species (N_2O and/or N_2) by denitrification and/or anammox with large isotope effects ($\varepsilon_{\text{nitrate-dinitrogen}} \sim +15$ to +30‰ for denitrification and anammox; Mariotti et al., 1981; Thunell et al., 2004; Fuchsman et al., 2008; Granger et al., 2008; Brunner et al., 2013; Wenk et al., 2014). Specifically, a suboxic zone can be easily established if the oxygen content of the water column is low. The residual NO_3^- is enriched in ^{15}N, with a magnitude depending on the residual fraction and N isotope enrichment factor (ε) during denitrification and/or anammox. From the present data, the signatures of $\delta^{15}N$ values in T2 (avg. + 1.5‰) and T3 (avg. + 8.6‰) sediments are considered as the most primary and reliable records of organic matter deposited in the Turee Creek basin. During T2 sediments deposition, the contribution of sedimentary organic N derived from NO_3^- assimilation was limited, due to a low NO_3^- availability. In contrast, the positive and only slightly variable $\delta^{15}N$ values of T3 likely reflect a stable pool of ^{15}N-enriched NO_3^-, which was assimilated by living organisms. Considering the similar C_{org}/N_{bulk} in T2 (avg. 28) and T3 (avg. 24) sediments, diagenetic and metamorphic effects on N isotope composition along with organic matter degradation should also be analogous. As a first approximation, we can consider the $\delta^{15}N$ value of +1.5‰ in T2 as representative of N isotope composition of organic matter from N_2-fixers after limited diagenesis and metamorphism. We can further assume that the minimum $\delta^{15}N$ value of dissolved NO_3^- during T3 deposition is around +7.0‰, under similar isotopic effect of diagenesis and metamorphism. If the fraction

of nitrate-users in T3 organic matter is not 100% and N_2-fixers represent a significant fraction of the total N isotope composition analyzed in bulk rock, the N isotope composition of dissolved NO_3^- recorded in T3 sediments should be higher.

The average NO_3^- concentration in surface water can be calculated from $\delta^{15}N$ value of NO_3^- and N isotope enrichment factors (Brandes et al., 1998; Voss et al., 2001) when the average phosphorus concentration in surface water is known. Moreover, dissolved oxygen concentration in surface waters can also be estimated based on the relationships between dissolved oxygen, aerobic mineralization, nitrate production and denitrification/anammox. Detailed calculations are presented and discussed in the following sections.

5.5.1. Dissolved nitrate concentration

In water column, N and P generally follow a stoichiometric relation, due to identical release rates of N and P from sinking particles of decomposing organic matter, which always contains N and P in a Redfield ratio (*i.e.* 16; Gruber and Deutsch, 2014). However, dissolved nitrate in low oxygen zone is usually depleted relative to phosphate (low $[NO_3^-]/[PO_4^{3-}]$ ratio) due to the loss of fixed nitrogen *via* denitrification and/or anammox. The denitrification and anammox lead to significant increase in $\delta^{15}N$ of the residual nitrate (Wada and Hattori, 1976), depending on the fraction of residual nitrate (Brandes et al., 1998; Voss et al., 2001). Therefore, we can calculate the fraction of residual nitrate (f) using a Rayleigh equation, based on $\delta^{15}N$ value of nitrate and N isotope enrichment factor (ε) during denitrification and/or anammox,

$$\delta^{15}N(initial\ nitrate) - \delta^{15}N(residual\ nitrate) = \varepsilon \times ln\ f \quad (1)$$

where $\delta^{15}N$ value of initial nitrate is assumed as 0‰ after quantitative mineralization and nitrification of organic matter from N_2-fixers. Then the average concentration of residual nitrate in surface seawater is related to the dissolved phosphate concentration by the relation (Cline and Richards, 1972; Voss et al., 2001),

$$f = NO_3^-(dissolved)/[R_{N:P} \times PO_4^{3-}(dissolved)] \quad (2)$$

where $R_{N:P}$ is the Redfield ratio of N over P, and NO_3^- and PO_4^{3-} are average dissolved nitrate and phosphate concentrations in surface seawater. Therefore dissolved nitrate concentration can be calculated if the dissolved phosphate concentration is known. Although dissolved phosphate concentration in Turee Creek paleo-seawater is unknown, we estimated the possible range from bulk rock data available for the Boolgeeda Iron Formation, underlying the Turee Creek Group (T1 drill core, see Fig. 1). We adopted the method developed by Bjerrum and Canfield (2002), based on the phosphorus and ferric iron contents of Archaean and early Proterozoic banded iron formation (BIF), and the adsorption properties of phosphorus on iron oxides such that,

$$PO_4^{3-}(dissolved) = (1/K_{ads}) \times (P_{ads}/Fe_{tot})/(Fe^{3+}/Fe_{tot}) \quad (3)$$

where K_{ads} (μM^{-1}) is the adsorption constant of phosphorus on iron oxides, P_{ads} (μM) is the concentration of phosphate adsorbed onto iron oxide particles, Fe^{3+} and Fe_{tot} are the ferric iron and total iron concentrations in BIFs. The adsorption constant (K_{ads}) can be influenced by solution chemistry such as salinity, as well as silica and divalent cations concentration (Konhauser et al., 2007; Jones et al., 2015). A reasonable range of K_{ads} from 0.048 to 0.139 can be considered for silica concentration from 1.5 to 0.6 mM, and modelled divalent concentrations at ~2.3 Ga (see for instance supplementary material in Jones et al., 2015). Based on selected parameters from previous studies and our data on Boolgeeda Iron Formation (Fig. 8 and Table 3), we estimated the dissolved phosphate concentration of seawater, in which Boolgeeda Iron Formation was deposited, to a range comprised between ~0.08 to 0.24 μM for K_{ads} of 0.139 and 0.048 respectively. These phosphate concentrations may be underestimated because up to 50% of the phosphorus might have been lost from Fe oxyhydroxides during early diagenesis (Bjerrum and Canfield, 2002; Jones et al., 2015). Moreover, the Boolgeeda Iron Formation represents the base of the Kungarra Formation and may not be perfectly representative of the T3 sediments (see Fig. 3 for a stratigraphic distribution of T1, T2 and T3). The phosphate concentration determined here probably represents a lower limit for the depositional environment of T3 shales and carbonates because of higher removal capacity of phosphorus by Fe oxyhydroxides in the Boolgeeda Iron Formation. A higher dissolved phosphate concentration in T3 seawater relative to T1 (Boolgeeda) is consistent with the higher TOC content in T3 samples (TOC ~ 685 ppm) than in T1 samples (TOC ~ 133 ppm). Overall, we conclude that the range of phosphate concentrations calculated from BIFs (~0.08 to 0.24 μM) can be regarded as a lower limit for the seawater corresponding to T3 sediments deposition.

Using this range of phosphate concentrations, dissolved nitrate can be estimated from Eqs. (1) and (2). The results are illustrated in Fig. 9a and represent an upper limit of dissolved NO_3^- concentration in T3 paleo-water column. The dissolved nitrate concentration in surface water should have ranged below 1.91 to 3.04 μM ($\delta^{15}N_{dissolved\ nitrate} = +7.0‰$, $K_{ads} = 0.048$; Fig. 9a) depending on the isotope enrichment factor (ε). This calculation assumes $\delta^{15}N_{dissolved\ nitrate}$ of +7‰ and thus that the fraction of nitrate-using organisms in sedimentary organic matter is 100%. A smaller fraction of only 60% (*i.e.* with 40% N_2-fixers) is also reported for comparison by considering $\delta^{15}N_{dissolved\ nitrate}$ of +12‰ (Fig. 9a). This shows that dissolved NO_3^- concentration would be lower, in a range between 1.16 and 2.57 μM ($\delta^{15}N_{dissolved\ nitrate} = +12‰$, $K_{ads} = 0.048$; Fig. 9a). For lower phosphate concentration (and $K_{ads} = 0.139$), the model predicts dissolved NO_3^- concentration from 0.39 to 0.86 μM. We conclude that reasonable estimate of the dissolved NO_3^- concentration in T3 paleo-water column may have been at the micromolar level, with values in a range from 0.5 to 3 μM.

5.5.2. Dissolved oxygen concentration

Assuming that N cycle in seawater is near steady state, we can consider that the size of the nitrate reservoir is stable, implying that input flux (*i.e.* nitrification) is equal to output flux (*i.e.* denitrification and/or anammox). The flux of nitrate production in surface water is related to oxygen consumption through aerobic mineralization of organic matter. The relation can be described as:

$$(CH_2O)_{106}(NH_3)_{16}(H_3PO_4) + 138O_2 \rightarrow 106CO_2 + 16HNO_3 + H_3PO_4 + 122H_2O \quad (4)$$

This equation illustrates that during the aerobic mineralization of 1 mol of organic matter, 138 mol of oxygen are required and 16 mol of nitrate are produced, according to the Redfield stoichiometry of organic matter (Redfield et al., 1963). Therefore, we can relate the nitrate input flux to the consumption of dissolved oxygen (*i.e.* downward flux from surface to deep waters where oxygen content is zero). Our approach does not discriminate, but includes, any type of organic matter produced by either oxygenic or anoxygenic photosynthesis. As nitrate in oxic water diffuses steadily into denitrification zone (suboxic zone in Fig. 7), specific N isotopic signature in residual nitrate is produced and depends on the residual fraction of nitrate during denitrification and/or anammox. Finally, residual nitrate with specific N isotopic signature is continually accumulated at depth and mixes with the surface nitrate pool. At near-steady state, we can write the two equations derived from Fick's law as follow:

$$F_{input} = -D_{O2} \times [C_{O2}/Z_1]/R_{O2:NO3-} = F_{output} \quad (5)$$

$$F_{down-diffusion} = -D_{NO3} \times [C_{NO3-}/Z_2] = F_{output}/(1-f) \quad (6)$$

where F_{input} is the input flux of new nitrate produced by aerobic degradation, F_{output} is the output flux by denitrification and/or anammox, $F_{down\text{-}diffusion}$ is the down-diffusion flux of nitrate from surface water to the redox boundary, D_{O2} and D_{NO3} are the diffusion coefficients of oxygen and nitrate in seawater, C_{O2} and C_{NO3-} are maximum dissolved oxygen and nitrate concentrations in surface oxic water, Z_1 is the distance between the depth with maximum O_2 concentration and the depth where oxygen concentration is zero, Z_2 is the distance between the depth with maximum NO_3^- concentration and the depth where NO_3^- concentration is zero, $R_{O2:NO3-}$ is the consumed oxygen amount when 1 mol nitrate is produced, and f is the fraction of residual nitrate after denitrification and/or anammox (as in Section 5.5.1). By coupling Eqs. (5) and (6), and assuming that Z_1 is equal to Z_2, the dissolved oxygen concentration (Fig. 9b) can thus be calculated as:

$$C_{O2} = [D_{NO3-}/D_{O2}] \times C_{NO3-} \times R_{O2:NO3-} \times (1-f) \quad (7)$$

A strong assumption of the present model is that ocean circulation is approximated only by diffusion. Although advection should also be important to consider, we note that in widespread marine environment like the Black Sea, dissolved NO_3^- concentration in the water column decreases linearly with depth and is consistent with a diffusion profile (Murray et al., 2005). Moreover, simulated oxygen profiles in the Black Sea are also compatible with diffusion from the Cold Intermediate Layer, which is the only oxygen source in the upper water column for the lower oxycline layer (Konovalov et al., 2006). It is unknown if the Turee Creek basin was similar to the Black Sea but we assume here that dissolved NO_3^- and O_2 concentrations are reasonably approximated by diffusive fluxes, at least at first order. The diffusion coefficients of oxygen and nitrate in seawater both depend on temperature. In the present model, we used two extreme diffusion coefficients by considering minimum and maximum temperatures of 0 and 24 °C, respectively, thus covering a wide range of temperature including cold ones corresponding to glacial sediments deposition. The dissolved oxygen concentration calculated here represents a minimum value for at least three reasons. Firstly, Z_1 is greater than or equal to Z_2 (Fig. 7), as supported by data from literature (Velinsky et al., 1991; Murray et al., 2005 and references therein). These previous studies demonstrated that Z_1/Z_2 ratio ranges from 1.5 to 5 in various redox-stratified aquatic systems. Secondly, the nitrate concentration (C_{NO3-}) calculated from average phosphate concentration represent a minimum value (see Section 5.5.1). Lastly, the model considers that O_2 is consumed only during organic matter mineralization by nitrification but neglects the potential effect of other reduced species such as Mn(II) and Fe(II). Therefore O_2 concentration calculated here from N isotope signature in TCDP sediments represents a minimum estimate. Another limit of our approach is that the dynamic of water masses such as advection is not taken into account in our simple approach. This will need to be tested in more complex models in the future.

The results of the calculation for dissolved oxygen concentration are presented in Fig. 9b. The lower limit of oxygen concentration in surface water would range from 1.8 to 4.4 μM ($\delta^{15}N_{dissolved\ nitrate} = +7.0‰$, $K_{ads} = 0.139$; Fig. 9b). If the fraction of nitrate-using organisms were not 100% or the value of K_{ads} were lower than 0.139, the calculated O_2 concentration would be higher (Fig. 9b). Assuming that dissolved oxygen in seawater was in equilibrium with the atmosphere, then atmospheric oxygen content could have reached ~0.9 to 2.1%PAL (Present Atmospheric Level)

during T3 sediment deposition. This estimate of atmospheric O_2 level is consistent with common values $> 10^{-2}$ PAL O_2 proposed for the Great Oxidation Event (*e.g.* Farquhar, 2000; Pavlov and Kasting, 2002; Kump, 2008). However this value of atmospheric O_2 content is uncertain since there is no evidence that Turee Creek marine waters were equilibrated with the atmosphere. In any case, our calculation provides a first-order estimate of dissolved nitrate and oxygen concentration in the Turee Creek basin.

In a redox transition period, O_2 produced by photosynthesis was released from the ocean to the atmosphere continuously and accumulated when the source exceeded the sink (Canfield et al., 2010). When atmospheric O_2 content reached a threshold level, then global aerobic nitrogen cycle could have been recorded in sedimentary rocks (e.g. Kipp et al., 2018). Based on U-Pb analyses on zircon and data from the literature, Caquineau et al. (2018) determined ages of the Turee Creek Group and found similar sedimentation rates in T2 and T3 of ~15 m/Ma. Using the correlation between sedimentation rate and organic matter concentration of modern oceanic sediments (Müller and Suess, 1979), one would expect C_{org} content of ~0.6 wt.% in the Turee Creek sediments for similar organic matter production, although a part of this C may have been lost during burial. Moreover, since organic matter mineralization was possibly less efficient in an O_2-poor world 2.3 Ga ago (*e.g.* Catling, 2014), a productivity similar to modern environments should have led to even higher C_{org} content (*i.e.* >0.6 wt.%). These observations suggest that the low TOC content of Turee Creek sediments (783 ± 332 ppm in T2 and 567 ± 307 ppm in T3) reflects a limited productivity, possibly ~10 times lower than modern oceanic productivity. A low productivity implies that NO_3^- biological demand was weak and may therefore explain partly why NO_3^- concentration and isotope composition were near steady state in the Turee Creek water column. However, an extremely low productivity would also provide small amount of O_2 in the photic zone and would thus hardly maintain a steady aerobic nitrogen cycle. Accordingly, the relatively stable $\delta^{15}N$ signal recorded in T3 sediments (~+8.6‰) may record the first global aerobic nitrogen cycle and the irreversible increase of O_2 necessary for nitrate stability in marine shallow waters between ~2.31 and ~2.25 Ga ago, possibly reflecting an early stage of the Lomagundi Event (~2.3 to ~2.1 Ga; Bachan and Kump, 2015). This finding is consistent and temporally concordant with inferences from N isotope compositions of the Rooihoogte and Timeball Hill formations in South Africa (Luo et al., 2018), suggesting global rather than local phenomena (see also Kipp et al., 2018).

6. CONCLUSION

In the present study, we combined C and N isotope analyses with major element chemistry in order to distinguish primary N isotope signature from detrital influence and post-depositional overprints and finally reconstruct paleoenvironmental conditions. The primary N isotope signature in Turee Creek sediments (~2.31 to ~2.25 Ga) significantly increased from about +1.5‰ in T2 to +8.6‰ in T3 samples. This suggests that higher dissolved oxygen concentration in T3 seawater promoted NO_3^- accumulation and associated partial denitrification, which allowed organisms to record heavier N isotope signature, then transferred to sediments. The limited variability of $\delta^{15}N$ values during deposition of T3 sediments suggests that N isotope cycle in Turee Creek basin was near steady state. This allowed us to evaluate dissolved nitrate and oxygen concentrations in surface water. A Rayleigh model for N isotope cycle suggests that the upper limit of average dissolved NO_3^- concentration ranges from 1.91 to 3.04 μM. A simple model for N isotope geochemical cycle under near-steady state regime shows that the lower limit of dissolved oxygen concentration in surface waters possibly ranged between 1.8 and 4.4 μM, consistent with oxygenated conditions at the time of T3 sediments deposition (~2.25 Ga ago). We conclude that Turee Creek sediments record a stepwise increase and accumulation of O_2 content in oceanic and possibly atmospheric reservoirs over one to several tens of millions of years.

ACKNOWLEDGMENTS

Wafa Abouchami, Stefan Lalonde, Bryan Killingsworth and colleagues from the laboratory of Stable Isotope Geochemistry in IPGP are thanked for fruitful discussions. This work was funded by the UnivEarths Labex programme at Sorbonne Paris Cité (ANR-10-LABX-0023 and ANR-11-IDEX-0005-02). Chen Cheng thanks the financial support of CSC scholarship (No. 201506430017) for studying in France. Vincent Busigny thanks the Institut Universitaire de France for funding (IUF #2017-2021). Pascal Philippot acknowledges support from the São Paulo Research Foundation (FAPESP, grant 2015/16235-2). Eva Stüeken, two anonymous reviewers, and Aubrey Zerkle (AE) are greatly thanked for detailed comments that strongly improved the paper. This is IPGP contribution No. XXX.

REFERENCES

Ader M., Macouin M., Hadrien M. H., Yang Z., Zhimming S. and Besse J. (2006) The Neoproterozoic carbon isotope excursions of the Doushantuo formation (South China) viewed from organic carbon isotope systematics. *Geochim. Cosmochim. Acta* **70**, A3.

Ader M., Sansjofre P., Halverson G. P., Busigny V., Trindade R. I. F., Kunzmann M. and Nogueira A. C. R. (2014) Ocean redox structure across the Late Neoproterozoic Oxygenation Event: A nitrogen isotope perspective. *Earth Planet. Sci. Lett.* **396**, 1–13.

Ader M., Thomazo C., Sansjofre P., Busigny V., Papineau D., Laffont R., Cartigny P. and Halverson G. P. (2016) Interpretation of the nitrogen isotopic composition of Precambrian sedimentary rocks: Assumptions and perspectives. *Chem. Geol.* **429**, 93–110.

Anbar A. D. and Knoll A. H. (2002) Proterozoic ocean chemistry and evolution: A bioinorganic bridge? *Science* **297**, 1137–1142.

Bachan A. and Kump L. R. (2015) The rise of oxygen and siderite oxidation during the Lomagundi event. *Proc. Natl. Acad. Sci.* **112**, 6562–6567.

Beaumont V. and Robert F. (1999) Nitrogen isotope ratios of kerogens in Precambrian cherts: a record of the evolution of atmosphere chemistry? *Precambr. Res.* **96**, 63–82.

Bebout G. E., Fogel M. L. and Cartigny P. (2013) Nitrogen: Highly volatile yet surprisingly compatible. *Elements* **9**, 333–338.

Bekker A., Holland H. D., Wang P.-L., Rumble D., Stein H. J., Hannah J. L., Coetzee L. L. and Beukes N. J. (2004) Dating the rise of atmospheric oxygen. *Nature* **427**, 117–120.

Bekker A., Holmden C., Beukes N. J., Kenig F., Eglingtone B. and Patterson W. P. (2008) Fractionation between inorganic and organic carbon during the Lomagundi (2.22–2.1 Ga) carbon isotope excursion. *Earth Planet. Sci. Lett.* **271**, 278–291.

Bjerrum C. J. and Canfield D. E. (2002) Ocean productivity before about 1.9 Gyr ago limited by phosphorus adsorption onto iron oxides. *Nature* **417**, 159–162.

Brandes J. A. and Devol A. H. (2002) A global marine-fixed nitrogen isotopic budget: Implications for Holocene nitrogen cycling. *Global Biogeochem. Cycles* **16**, 67-1-67–14.

Brandes J. A., Devol A. H., Yoshinari T., Jayakumar D. A. and Naqvi S. W. A. (1998) Isotopic composition of nitrate in the central Arabian Sea and eastern tropical North Pacific: A tracer for mixing and nitrogen cycles. *Limnol. Oceanogr.* **43**, 1680–1689.

Broecker W. S. and Peng T.-H. (1974) Gas exchange rates between air and sea. *Tellus* **26**, 21–35.

Busigny V., Ader M. and Cartigny P. (2005) Quantification and isotopic analysis of nitrogen in rocks at the ppm level using sealed tube combustion technique: A prelude to the study of altered oceanic crust. *Chem. Geol.* **223**, 249–258.

Busigny V., Lebeau O., Ader M., Krapež B. and Bekker A. (2013) Nitrogen cycle in the Late Archean ferruginous ocean. *Chem. Geol.* **362**, 115–130.

Canfield D. E., Raiswell R., Westrich J. T., Reaves C. M. and Berner R. A. (1986) The use of chromium reduction in the analysis of reduced inorganic sulfur in sediments and shales. *Chem. Geol.* **54**, 149–155.

Canfield D. E., Raiswell R. and Bottrell S. H. (1992) The reactivity of sedimentary iron minerals toward sulfide. *Am. J. Sci.* **292**, 659–683.

Canfield D. E., Glazer A. N. and Falkowski P. G. (2010) The evolution and future of earth's nitrogen cycle. *Science* **330**, 192–196.

Catling D. C. (2014) The great oxidation event transition. In *Treatise on Geochemistry* (eds. H. D. Holland and K. K. Turekian), second ed. Elsevier, Oxford, pp. 177–195.

Caquineau T., Paquette J.-L. and Philippot P. (2018) U-Pb detrital zircon geochronology of the Turee Creek Group, Hamersley Basin, Western Australia: Timing and correlation of the Paleoproterozoic glaciations. *Precambr. Res.* **307**, 34–50.

Caquineau T., Paquette J. L. and Philippot P. (2019) Hf isotope provenance analysis of the Turee Creek Group (Pilbara Craton, Western Australia): implications on the rise of atmospheric oxygen and global glaciation during the Paleoproterozoic. *Earth Planet. Sci. Lett.*, in preparation.

Carignan J., Hild P., Mevelle G., Morel J. and Yeghicheyan D. (2001) Routine analyses of trace elements in geological samples using flow injection and low pressure on-line liquid chromatography coupled to ICP-MS: A study of geochemical reference materials BR, DR-N, UB-N, AN-G and GH. *Geostand. Geoanal. Res.* **25**, 187–198.

Chang B. X. and Devol A. H. (2009) Seasonal and spatial patterns of sedimentary denitrification rates in the Chukchi sea. *Deep Sea Res. Part II* **56**, 1339–1350.

Cline J. D. and Richards F. A. (1972) Oxygen deficient conditions and nitrate reduction in the eastern tropical North Pacific Ocean. *Limnol. Oceanogr.* **17**, 885–900.

Farquhar J. (2000) Atmospheric influence of Earth's earliest sulfur cycle. *Science* **289**, 756–758.

Fennel K. (2005) The co-evolution of the nitrogen, carbon and oxygen cycles in the Proterozoic ocean. *Am. J. Sci.* **305**, 526–545.

Fuchsman C. A., Murray J. W. and Konovalov S. K. (2008) Concentration and natural stable isotope profiles of nitrogen species in the Black Sea. *Mar. Chem.* **111**, 90–105.

Galbraith E. D., Sigman D. M., Robinson R. S. and Pedersen T. F. (2008) Nitrogen in past marine environments. In *Nitrogen in the Marine Environment* (eds. D. G. Capone, D. A. Bronk, M. R. Mulholland and E. J. Carpenter). Elsevier Academic Press, pp. 1497–1535.

Garvin J., Buick R., Anbar A. D., Arnold G. L. and Kaufman A. J. (2009) Isotopic evidence for an aerobic nitrogen cycle in the latest archean. *Science* **323**, 1045–1048.

Gilleaudeau G. J. and Kah L. C. (2013) Carbon isotope records in a Mesoproterozoic epicratonic sea: Carbon cycling in a low-oxygen world. *Precambr. Res.* **228**, 85–101.

Godfrey L. V. and Falkowski P. G. (2009) The cycling and redox state of nitrogen in the Archaean ocean. *Nat. Geosci.* **2**, 725–729.

Godfrey L. V., Poulton S. W., Bebout G. E. and Fralick P. W. (2013) Stability of the nitrogen cycle during development of sulfidic water in the redox-stratified late Paleoproterozoic Ocean. *Geology* **41**, 655–658.

Goldblatt C., Lenton T. M. and Watson A. J. (2006) Bistability of atmospheric oxygen and the great oxidation. *Nature* **443**, 683–686.

Goldblatt C., Claire M. W., Lenton T. M., Matthews A. J., Watson A. J. and Zahnle K. J. (2009) Nitrogen-enhanced greenhouse warming on early Earth. *Nat. Geosci.* **2**, 891–896.

Granger J., Sigman D. M., Lehmann M. F. and Tortell P. D. (2008) Nitrogen and oxygen isotope fractionation during dissimilatory nitrate reduction by denitrifying bacteria. *Limnol. Oceanogr.* **53**, 2533–2545.

Gruber N. and Deutsch C. A. (2014) Redfield's evolving legacy. *Nat. Geosci.* **7**, 853–855.

Guo H., Du Y., Kah L., Huang J., Hu C., Huang H. and Yu W. (2013) Isotopic composition of organic and inorganic carbon from the Mesoproterozoic Jixian Group, North China: Implications for biological and oceanic evolution. *Precambr. Res.* **224**, 169–183.

Hayes J. M., Strauss H. and Kaufman A. J. (1999) The abundance of ^{13}C in marine organic matter and isotopic fractionation in the global biogeochemical cycle of carbon during the past 800 Ma. *Chem. Geol.* **161**, 103–125.

Hedges J. I. and Keil R. G. (1995) Sedimentary organic matter preservation: an assessment and speculative synthesis. *Mar. Chem.* **49**, 81–115.

Honma H. and Itihara Y. (1981) Distribution of ammonium in minerals of metamorphic and granitic rocks. *Geochim. Cosmochim. Acta* **45**, 983–988.

Ishida A., Hashizume K. and Kakegawa T. (2017) Microbial nitrogen cycle enhanced by continental input recorded in the gunflint formation. *Geochemical Perspectives Letters* **4**, 13–18.

Izon G., Zerkle A. L., Williford K. H., Farquhar J., Poulton S. W. and Claire M. W. (2017) Biological regulation of atmospheric chemistry en route to planetary oxygenation. *Proc. Natl. Acad. Sci.* **114**, E2571–E2579.

Jia Y. and Kerrich R. (2004) Nitrogen 15-enriched Precambrian kerogen and hydrothermal systems: Kerogen and vein systems. *Geochem. Geophys. Geosyst.* **5**, Q07005. https://doi.org/10.1029/2004GC000716.

Jones C., Nomosatryo S., Crowe S. A., Bjerrum C. J. and Canfield D. E. (2015) Iron oxides, divalent cations, silica, and the early earth phosphorus crisis. *Geology* **43**, 135–138.

Kah L. C. and Bartley J. K. (2011) Protracted oxygenation of the Proterozoic biosphere. *Int. Geol. Rev.* **53**, 1424–1442.

UNCORRECTED PROOF

Kendall B., Brennecka G. A., Weyer S. and Anbar A. D. (2013) Uranium isotope fractionation suggests oxidative uranium mobilization at 2.50 Ga. *Chem. Geol.* **362**, 105–114.

Kipp M. A., Stüeken E. E., Yun M., Bekker A. and Buick R. (2018) Pervasive aerobic nitrogen cycling in the surface ocean across the Paleoproterozoic Era. *Earth Planet. Sci. Lett.* **500**, 117–126.

Knoll A. H. and Nowak M. A. (2017) The timetable of evolution. *Sci. Adv.* **3**, e1603076.

Koehler M. C., Stueeken E. E., Kipp M. A., Buick R. and Knoll A. H. (2017) Spatial and temporal trends in Precambrian nitrogen cycling: A Mesoproterozoic offshore nitrate minimum. *Geochim. Cosmochim. Acta* **198**, 315–337.

Konhauser K. O., Lalonde S. V., Amskold L. and Holland H. D. (2007) Was there really an archean phosphate crisis? *Science* **315**, 1234–1234.

Konovalov S. K., Murray J. W., Luther G. W. and Tebo B. M. (2006) Processes controlling the redox budget for the oxic/anoxic water column of the Black Sea. *Deep Sea Res. Part II* **53**, 1817–1841.

Kump L. R. (2008) The rise of atmospheric oxygen. *Nature* **451**, 277–278.

Kump L. R., Junium C., Arthur M. A., Brasier A., Fallick A., Melezhik V., Lepland A., Crne A. E. and Luo G. (2011) Isotopic evidence for massive oxidation of organic matter following the great oxidation event. *Science* **334**, 1694–1696.

Lam P. and Kuypers M. M. (2011) Microbial nitrogen cycling processes in oxygen minimum zones. *Ann. Rev. Mar. Sci.* **3**, 317–345.

Li L., Sherwood Lollar B., Li H., Wortmann U. G. and Lacrampe-Couloume G. (2012) Ammonium stability and nitrogen isotope fractionations for NH_4^+ –$NH_{3(aq)}$–$NH_{3(gas)}$ systems at 20–70 °C and pH of 2–13: Applications to habitability and nitrogen cycling in low-temperature hydrothermal systems. *Geochim. Cosmochim. Acta* **84**, 280–296.

Luo G., Junium C. K., Kump L. R., Huang J., Li C., Feng Q., Shi X., Bai X. and Xie S. (2014) Shallow stratification prevailed for ~1700 to ~1300Ma ocean: Evidence from organic carbon isotopes in the North China Craton. *Earth Planet. Sci. Lett.* **400**, 219–232.

Luo G., Ono S., Beukes N. J., Wang D. T., Xie S. and Summons R. E. (2016) Rapid oxygenation of Earth's atmosphere 2.33 billion years ago. *Sci. Adv.* **2**. https://doi.org/10.1126/sciadv.1600134.

Luo G., Junium C. K., Izon G., Ono S., Beukes N. J., Algeo T. J., Cui Y., Xie S. and Summons R. E. (2018) Nitrogen fixation sustained productivity in the wake of the palaeoproterozoic great oxygenation event. *Nat. Commun.* **9**, 1–9.

Lyons T. W. and Severmann S. (2006) A critical look at iron paleoredox proxies: New insights from modern euxinic marine basins. *Geochim. Cosmochim. Acta* **70**, 5698–5722.

Lyons T. W., Reinhard C. T. and Planavsky N. J. (2014) The rise of oxygen in Earth's early ocean and atmosphere. *Nature* **506**, 307–315.

Mariotti A., Germon J. C., Hubert P., Kaiser P., Letolle R., Tardieux A. and Tardieux P. (1981) Experimental determination of nitrogen kinetic isotope fractionation: Some principles; illustration for the denitrification and nitrification processes. *Plant Soil* **62**, 413–430.

Martin D. M. (1999) Depositional setting and implications of Paleoproterozoic glaciomarine sedimentation in the Hamersley Province, Western Australia. *Geol. Soc. Am. Bull.* **111**, 189–203.

Martindale R. C., Strauss J. V., Sperling E. A., Johnson J. E., Van Kranendonk M. J., Flannery D., French K., Lepot K., Mazumder R., Rice M. S., Schrag D. P., Summons R., Walter M., Abelson J. and Knoll A. H. (2015) Sedimentology, chemostratigraphy, and stromatolites of lower Paleoproterozoic carbonates, Turee Creek Group, Western Australia. *Precambr. Res.* **266**, 194–211.

Mazumder R., Van Kranendonk M. J. and Altermann W. (2015) A marine to fluvial transition in the Paleoproterozoic Koolbye Formation, Turee Creek Group, Western Australia. *Precambr. Res.* **258**, 161–170. https://doi.org/10.1016/j.precamres.2014.12.005.

Minagawa M. and Wada E. (1986) Nitrogen isotope ratios of red tide organisms in the East China Sea: A characterization of biological nitrogen fixation. *Mar. Chem.* **19**, 245–259.

Mook W. G., Bommerson J. C. and Staverman W. H. (1974) Carbon isotope fractionation between dissolved bicarbonate and gaseous carbon dioxide. *Earth Planet. Sci. Lett.* **22**, 169–176.

Müller P. J. and Suess E. (1979) Productivity, sedimentation rate, and sedimentary organic matter in the oceans—I. Organic carbon preservation. Deep Sea Research Part A. *Oceanographic Res. Pap.* **26**, 1347–1362.

Muller E., Thomazo C., Stüeken E. E., Hallmann C., Leiderd A., Chaduteau C., Buick R., Baton F., Philippot P. and Ader M. (2018) Bias in carbon concentration and δ13C measurements of organic matter due to cleaning treatments with organic solvents. *Chem. Geol.* **493**, 405–412.

Murray J., Fuchsman C., Kirkpatrick J., Paul B. and Konovalov S. (2005) Species and δ15N signatures of nitrogen transformations in the suboxic zone of the Black Sea. *Oceanography* **18**, 36–47.

Papineau D., Purohit R., Goldberg T., Pi D., Shields G. A., Bhu H., Steele A. and Fogel M. L. (2009) High primary productivity and nitrogen cycling after the Paleoproterozoic phosphogenic event in the Aravalli Supergroup, India. *Precambr. Res.* **171**, 37–56.

Papineau D., Purohit R., Fogel M. L. and Shields-Zhou G. A. (2013) High phosphate availability as a possible cause for massive cyanobacterial production of oxygen in the Paleoproterozoic atmosphere. *Earth Planet. Sci. Lett.* **362**, 225–236.

Pavlov A. A. and Kasting J. F. (2002) Mass-independent fractionation of sulfur isotopes in Archean sediments: strong evidence for an anoxic archean atmosphere. *Astrobiology* **2**, 27–41.

Philippot P., Avila J., Lillingsworth B., Tessalina S., Baton F., Caquineau T., Muller E., Pecoits E., Cartigny P., Lalonde S., Ireland T., Thomazo C., van Kranendonk M. and Busigny V. (2018) Globally asynchronous sulphur isotope signals require re-definition of the great oxidation event. *Nat. Commun.* **9**. https://doi.org/10.1038/s41467-018-04621-x.

Pinti D. L., Hashizume K. and Matsuda J. (2001) Nitrogen and argon signatures in 3.8 to 2.8 Ga metasediments: Clues on the chemical state of the Archean ocean and the deep biosphere. *Geochim. Cosmochim. Acta* **65**, 2301–2315.

Pinti D. L., Hashizume K., Sugihara A., Massault M. and Philippot P. (2009) Isotopic fractionation of nitrogen and carbon in Paleoarchean cherts from Pilbara craton, Western Australia: Origin of 15 N-depleted nitrogen. *Geochim. Cosmochim. Acta* **73**, 3819–3848.

Planavsky N. J., McGoldrick P., Scott C. T., Li C., Reinhard C. T., Kelly A. E., Chu X., Bekker A., Love G. D. and Lyons T. W. (2011) Widespread iron-rich conditions in the mid-Proterozoic ocean. *Nature* **477**, 448–451.

Planavsky N. J., Reinhard C. T., Wang X., Thomson D., McGoldrick P., Rainbird R. H., Johnson T., Fischer W. W. and Lyons T. W. (2014) Low Mid-Proterozoic atmospheric oxygen levels and the delayed rise of animals. *Science* **346**, 635–638.

Playter T., Konhauser K., Owttrim G., Hodgson C., Warchola T., Mloszewska M., Sutherland B., Bekker A., Zonneveld J.-P., George Pemberton S. and Gingras M. (2017) Microbe-clay interactions as a mechanism for the preservation of organic

UNCORRECTED PROOF

matter and trace metal biosignatures in black shales. *Chem. Geol.* **459**, 75–90.

Popp B. N., Laws E. A., Bidigare R. R., Dore J. E., Hanson K. L. and Wakeham S. G. (1998) Effect of Phytoplankton Cell Geometry on Carbon Isotopic Fractionation. *Geochim. Cosmochim. Acta* **62**, 69–77.

Poulton S. W., Krom M. D. and Raiswell R. (2004) A revised scheme for the reactivity of iron (oxyhydr)oxide minerals towards dissolved sulfide. *Geochim. Cosmochim. Acta* **68**, 3703–3715.

Poulton S. W. and Canfield D. E. (2005) Development of a sequential extraction procedure for iron: implications for iron partitioning in continentally derived particulates. *Chem. Geol.* **214**, 209–221.

Poulton S. W. and Canfield D. E. (2011) Ferruginous conditions: a dominant feature of the ocean through Earth's history. *Elements* **7**, 107–112.

Quan T. M., van de Schootbrugge B., Field M. P., Rosenthal Y. and Falkowski P. G. (2008) Nitrogen isotope and trace metal analyses from the Mingolsheim core (Germany): Evidence for redox variations across the Triassic-Jurassic boundary. *Global Biogeochem. Cycles* **22**, GB2014. https://doi.org/10.1029/2007GB002981.

Raiswell R., Newton R., Bottrell S. H., Coburn P., Briggs D. E. G., Bond D. P. G. and Poulton S. W. (2008) Turbidite depositional influences on the diagenesis of Beecher's Trilobite Bed and the Hunsruck Slate: sites of soft tissue pyritization. *Am. J. Sci.* **308**, 105–129.

Raiswell R. and Canfield D. E. (1998) Sources of iron for pyrite formation in marine sediments. *Am. J. Sci.* **298**, 219–245.

Rasmussen B., Blake T. S. and Fletcher I. R. (2005) U-Pb zircon age constraints on the Hamersley spherule beds: Evidence for a single 2.63 Ga Jeerinah-Carawine impact ejecta layer. *Geology* **33**, 725–728.

Redfield J. L., Ketchum B. H. and Rickards F. A. (1963) The influence of organisms on the composition of seawater. In *The Sea* (ed. M. N. Hill). John Wiley & Sons, New York, pp. 26–77.

Reuschel M., Melezhik V. and Strauss H. (2012) Sulfur isotopic trends and iron speciation from the c. 2.0 Ga Pilgujärvi sedimentary formation, NW Russia. *Precambr. Res.* **196**, 193–203.

Robinson R. S., Kienast M., Albuquerque A. L. and Altabet M., et al. (2012) A review of nitrogen isotopic alteration in marine sediments. *Paleoceanography* **27**. https://doi.org/10.1029/2012PA002321.

Rouchon V., Pinti D. L., Gallien J.-P., Orberger B., Daudin L. and Westall F. (2005) NRA analyses of N and C in hydromuscovite aggregates from a 3.5Ga chert from Kittys Gap, Pilbara, Australia. *Nucl. Instrum. Methods Phys. Res., Sect. B* **231**, 536–540.

Sansjofre P., Ader M., Trindade R. I. F., Elie M., Lyons J., Cartigny P. and Nogueira A. C. R. (2011) A carbon isotope challenge to the snowball Earth. *Nature* **478**, 93–96.

Sauvage L., Riquier L., Thomazo C., Baudin F. and Martinez M. (2013) The late Hauterivian Faraoni "Oceanic Anoxic Event" at Río Argos (southern Spain): an assessment on the level of oxygen depletion. *Chem. Geol.* **340**, 77–90.

Schidlowski M. (2001) Carbon isotopes as biogeochemical recorders of life over 3.8 Ga of Earth history: evolution of a concept. *Precambr. Res.* **106**, 117–134.

Sigman D. M., Karsh K. L. and Casciotti K. L. (2010) Nitrogen isotopes in the ocean. In *Encyclopedia of Ocean Sciences* (eds. J. H. Steele, S. A. Thorpe and K. K. Turekian). Academic Press, Oxford, pp. 40–54.

Smith R. E., Perdrix J. L. and Parks T. C. (1982) Burial metamorphism in the Hamersley basin, Western Australia. *J. Petrol.* **23**, 75–102.

Stüeken E. E. (2013) A test of the nitrogen-limitation hypothesis for retarded eukaryote radiation: Nitrogen isotopes across a Mesoproterozoic basinal profile. *Geochim. Cosmochim. Acta* **120**, 121–139.

Stüeken E. E., Buick R., Guy B. M. and Koehler M. C. (2015a) Isotopic evidence for biological nitrogen fixation by molybdenum-nitrogenase from 3.2 Gyr. *Nature* **520**, 666–669.

Stüeken E. E., Buick R. and Schauer A. J. (2015b) Nitrogen isotope evidence for alkaline lakes on late Archean continents. *Earth Planet. Sci. Lett.* **411**, 1–10.

Stüeken E. E., Kipp M. A., Koehler M. C. and Buick R. (2016) The evolution of Earth's biogeochemical nitrogen cycle. *Earth Sci. Rev.* **160**, 220–239.

Stüeken E. E., Buick R., Anderson R. E., Baross J. A., Planavsky N. J. and Lyons T. W. (2017) Environmental niches and metabolic diversity in Neoarchean lakes. *Geobiology* **15**, 767–783.

Taylor S. R. and McLennan S. M. (1985) *The Continental Crust: Its Composition and Evolution*. Blackwell, Oxford.

Tesdal J. E., Galbraith E. D. and Kienast M. (2013) Nitrogen isotopes in bulk marine sediment: linking seafloor observations with subseafloor records. *Biogeosciences* **10**, 101–118.

Thomazo C., Ader M. and Philippot P. (2011) Extreme ^{15}N-enrichments in 2.72 Gyr old sediments: evidence for a turning point in the nitrogen cycle. *Geobiology* **9**, 107–120.

Thomazo C. and Papineau D. (2013) Biogeochemical cycling of nitrogen on the early Earth. *Elements* **9**, 345–351.

Thunell R. C., Sigman D. M., Muller-Karger F., Astor Y. and Varela R. (2004) Nitrogen isotope dynamics of the Cariaco Basin, Venezuela. *Global Biogeochem. Cycles* **18**, GB3001. https://doi.org/10.1029/2003GB002185.

Trendall A. F., Compston W., Nelson D. R., De Laeter J. R. and Bennett V. C. (2004) SHRIMP zircon ages constraining the depositional chronology of the Hamersley Group, Western Australia. *Aust. J. Earth Sci.* **51**, 621–644.

Van Kranendonk M. J., Mazumder R., Yamaguchi K. E., Yamada K. and Ikehara M. (2015) Sedimentology of the Paleoproterozoic Kungarra Formation, Turee Creek Group, Western Australia: A conformable record of the transition from early to modern Earth. *Precambr. Res.* **256**, 314–343.

Velinsky D. J., Fogel M. L., Todd J. F. and Tebo B. M. (1991) Isotopic fractionation of dissolved ammonium at the oxygen-hydrogen sulfide interface in anoxic waters. *Geophys. Res. Lett.* **18**, 649–652.

Voss M., Dippner J. W. and Montoya J. P. (2001) Nitrogen isotope patterns in the oxygen-deficient waters of the Eastern Tropical North Pacific Ocean. *Deep Sea Res. Part I* **48**, 1905–1921.

Wada E. and Hattori A. (1976) Natural abundance of 15N in particulate organic matter in the North Pacific Ocean. *Geochim. Cosmochim. Acta* **40**, 249–251.

Wenk C. B., Zopfi J., Gardner W. S., McCarthy M. J., Niemann H., Veronesi M. and Lehmann M. F. (2014) Partitioning between benthic and pelagic nitrate reduction in the Lake Lugano south basin. *Limnol. Oceanogr.* **59**, 1421–1433.

Ye Q., Tong J., Tian L., Hu J., An Z., Bodnar R. J. and Xiao S. (2019) Detrital graphite particles in the Cryogenian Nantuo Formation of South China: Implications for sedimentary provenance and tectonic history. *Precambr. Res.* **323**, 6–15.

Zerkle A. L., Junium C. K., Canfield D. E. and House C. H. (2008) Production of 15 N-depleted biomass during cyanobacterial N 2 -fixation at high Fe concentrations. *J. Geophys. Res.* **113**. https://doi.org/10.1029/2007JG000651.

UNCORRECTED PROOF

Zerkle A. L., Poulton S. W., Newton R. J., Mettam C., Claire M. W., Bekker A. and Junium C. K. (2017) Onset of the aerobic nitrogen cycle during the Great Oxidation Event. *Nature* **542**, 465–467.

Zerkle A. and Mikhail S. (2017) The geobiological nitrogen cycle: From microbes to the mantle. *Geobiology* **15**, 343–352.

Zhang X., Sigman D. M., Morel F. M. M. and Kraepiel A. M. L. (2014) Nitrogen isotope fractionation by alternative nitrogenases and past ocean anoxia. *Proc. Natl. Acad. Sci.* **111**, 4782–4787.

Associate editor: Aubrey Zerkle